

Precision measurements of $A = 3$ nuclei in Hall B

A. Denniston, O. Hen (spokesperson), J. Kahlbow, D. Nguyen (spokesperson),
J. R. Pybus, E.P. Segarra,
Massachusetts Institute of Technology, Cambridge, Massachusetts 02139, USA

W. Briscoe, T. Kutz, S. Ratliff, A. Schmidt (spokesperson), P. Sharp, I. Strakovsky
The George Washington University, Washington DC 20052, USA

C. Fogler, F. Hauenstein, C. Hyde, L.B. Weinstein (spokesperson)
Old Dominion University, Norfolk, Virginia 23529, USA

G. Johansson, C. Neuburger, E. Piasetzky (spokesperson)
Tel-Aviv University, Tel Aviv 69978, Israel

D.W. Higinbotham, C. Keith, C. Keppel, J. Maxwell, D. Meekins (spokesperson),
S. Stepanyan, H. Szumila-Vance (contact person)
Thomas Jefferson National Accelerator Facility,
Newport News, Virginia 23606, USA

R. Cruz Torres
Lawrence Berkeley National Laboratory, Berkeley, California 94720, USA

A. Boyer, F. Benmokhtar, A. Gadsby, A. Parker
Duquesne University, Pittsburgh, PA 15208 USA

L. Baashen, B. Raue
Florida International University, Miami, FL 33199 USA

B. McKinnon
University of Glasgow, Glasgow, United Kingdom

W. Brooks
Universidad Técnica Federico Santa María, Valparaíso, Chile

A. Beck, S. Beck, I. Korover
Nuclear Research Center Negev, Be'er Sheva, Israel

Sheren Alsalmi
King Saud Univeristy, Riyadh, Saudi Arabia

M. Mihovilovič, S. Širca
University of Ljubljana, Jožef Stefan Institute, Ljubljana, Slovenia

C. Ayerbe, T. Chetry, D. Dutta, L. El Fassi
Mississippi State University, Mississippi State, MS 39762 USA

M. Osipenko
Istituto Nazionale di Fisica Nucleare, Sezione di Genova, Genoa, Italy

Eric Christy
Hampton University, Hampton, VA, 23669, USA

N. Gevorgyan, N. Dashyan
Yerevan Physics Institute, Yerevan, Armenia

Peter Monaghan
Christopher Newport University, Newport News, VA 23606, USA

R. Capobianco, S. Diehl, F.-X. Girod, K. Joo, A. Kim, V. Klimenko, R. Santos
University of Connecticut, Storrs, CT, USA

and the CLAS Collaboration

Abstract

We propose a high-statistics measurement of few body nuclear structure and short range correlations in quasi-elastic scattering at 6.6 GeV from ^2H , ^3He and ^3H targets in Hall B with the CLAS12 detector.

We will measure absolute cross sections for $(e, e'p)$ and $(e, e'pN)$ quasi-elastic reaction channels up to a missing momentum $p_{miss} \approx 1$ GeV/c over a wide range of Q^2 and x_B and construct the isoscalar sum of ^3H and ^3He . We will compare $(e, e'p)$ cross sections to nuclear theory predictions using a wide variety of techniques and NN interactions in order to constrain the NN interaction at short distances. We will measure $(e, e'pN)$ quasi-elastic reaction cross sections and $(e, e'pN)/(e, e'p)$ ratios to understand short range correlated (SRC) NN pairs in the simplest non-trivial system. ^3H and ^3He , being mirror nuclei, exploit the maximum available isospin asymmetry. They are light enough that their ground states are readily calculable, but they already exhibit complex nuclear behavior, including NN SRCs. We will also measure $d(e, e'p)$ in order to help theorists constrain non-quasielastic reaction mechanisms in order to better calculate reactions on $A = 3$ nuclei. Measuring all three few body nuclei together is critical, in order to understand and minimize different reaction effects, such as single charge exchange final state interactions, in order to test ground-state nuclear models.

We will also measure the ratio of inclusive (e, e') quasi-elastic cross sections (integrated over x_B) from ^3He and ^3H in order to extract the neutron magnetic form factor G_M^n at small and moderate values of Q^2 . We will measure this at both 6.6 GeV and 2.2 GeV.

Simulations and previous experience with CLAS12 show that we can obtain meaningful statistics with 55 days of beam time. We request 20 beam days each on ^3He and ^3H , and 10 beam days on ^2H at an incident beam energy of 6.6 GeV. We request an additional 5.5 days of beam time at 2.2 GeV to measure G_M^n at low Q^2 . Our proposed measurements will significantly constrain nuclear models for few body nuclear dynamics and short range structure. Also, we will measure the behavior of the neutron magnetic form factor at low to moderate Q^2 .

This experiment will use the base equipment for CLAS12 and requires the construction of a new ^3H target. The JLab Target Group has a preliminary target design. The groups working on this experiment bring previous experience working with a ^3H target in Hall A.

1 Introduction

We propose to measure quasi-elastic electron scattering on ^3He , ^3H , and deuterium targets in Hall B using the CLAS12 detector in its standard configuration (no forward tagger) with an open electron trigger. We will use a newly designed cryo-target that is specifically developed for the ^3H containment and safety considerations (designed and developed with previous experience from the Hall A ^3H measurements, see section 5). We will use identical cryo-target cells for the ^3H , ^3He , and ^2H targets. The CLAS12 detector can access a large range in x_B and Q^2 allowing us to measure reactions over a wide kinematic coverage. This will let us select kinematics where the effects of outgoing nucleon rescattering (final state interactions (FSI)) and other non-quasi-elastic reaction mechanisms are minimized.

The experiment will measure ^3He and $^3\text{H}(e, e'p)$ proton momentum distributions to extremely high missing momenta ($\vec{p}_{miss} = \vec{p}' - \vec{q}$, where \vec{q} is the three-momentum transfer and \vec{p}' is the outgoing proton momentum) in order to constrain the short distance behavior of models of the NN potential. It will also measure the other nucleons knocked out in the reaction using $(e, e'pp)$ and $(e, e'pn)$ to measure characteristics of nucleon-nucleon (NN) Short Range Correlations (SRC). These $A = 3$ mirror nuclei provide the maximum isospin asymmetry, coupled with theoretical calculability and minimal attenuation or rescattering of the outgoing hadrons. We will also measure $d(e, e'p)$ to constrain calculations of non-quasielastic reaction mechanisms on the simplest nucleus and to determine kinematics least sensitive to these effects. The combination of ^3He and ^3H is essential as theoretical predictions must be able to account for both. As will be discussed in Section 2, measurements of each individual $A = 3$ nuclei alone are insufficient without the other in order to fully constrain the NN interaction and decouple the contributions of FSIs.

In addition, we will measure quasi-elastic inclusive scattering on ${}^3\text{He}$ and ${}^3\text{H}$ to extract the neutron magnetic form factor G_M^n at low to moderate Q^2 . A short 2.2-GeV run will enable us to measure G_M^n at $Q^2 < 0.5$ $[\text{GeV}/c]^2$ where previous measurements are in contention with model predictions.

We build on the Letter Of Intent [1] that describes experimental possibilities with a ${}^3\text{H}$ target in Hall B, but we focus on quasi-elastic scattering. The CLAS12 detector is ideally-suited for these studies with only slightly lower luminosity than the previous Hall A measurements but significantly larger acceptance. The combination of luminosity and acceptance enable high statistics studies with access to a wide range of kinematical dependencies that will be able to precisely guide nuclear theory.

We present an overview of the current physics that is relevant to the measurements we will obtain in $A = 3$ nuclei in Section 2. We detail the physics goals in Section 3, and we discuss the measurements and relevant observables of the quasi-elastic reaction in detail in Section 4. Finally, we provide a description and plan for the design of the ${}^3\text{H}$ target (Section 5).

2 Overview of recent results

The fundamental dynamics of the nuclear many-body system has implications in other areas of physics from understanding astrophysical systems such as neutron stars to discerning the many body fermion systems in cold atomic physics. The nuclear few-body system allows us to test critical aspects of our understanding of many-body systems, specifically the NN interaction at short distances and the effects of short range correlated nucleon pairs. Nuclear few-body systems are relatively simple, calculable systems and measurements of these systems can provide precise tests of modern theories.

Quasi-elastic (QE) electron scattering is sensitive to the ground state properties of nuclei. For heavy nuclei, this sensitivity is difficult to evaluate due to imprecise nuclear ground state calculations and contributions from non-QE reactions. The non-QE contributions have significant and hard-to-quantify impacts on the measured cross sections. These contributions including final state interactions (FSIs), single charge exchange (SCX), meson exchange currents (MEC), and Δ production or isobar configurations (IC), are highly model-dependent and obscure the interpretation of data in terms of the nuclear ground state [2].

Studies of both ${}^3\text{He}$ and ${}^3\text{H}$ resolve the complications that arise when calculating heavier nuclei. They have exactly calculable ground states from nuclear-interaction models. Furthermore, the combination of measurements from ${}^3\text{He}$, ${}^3\text{H}$, and deuterium over a larger kinematic range can be used to uniquely disentangle the contributions from FSIs, optimize the kinematic selection for this reduction and thus enable one to directly relate measured cross-sections to the ground-state momentum distributions. Early studies on ${}^3\text{He}$ alone showed that we are sensitive to the ground state distributions and can make detailed comparisons with theory [3]. Here, the combination of studying ${}^3\text{He}$ and ${}^3\text{H}$ nuclei benchmark modern nuclear theory and place tight constraints.

Deuterium, ${}^3\text{He}$, and ${}^3\text{H}$ put to test the most fundamental descriptions of eA reactions, including how an electron interacts with an off-shell bound nucleon. Recent theoretical work [4] using light front calculations (i.e. light cone reference frame) provides techniques to reduce off-shell effects in the electron-bound-nucleon cross section at $Q^2 > 1$ GeV^2/c^2 to much less than in the standardly-used deForest prescriptions [5]. This effect is separate from bound nucleon modifications. We plan to work closely with theorists to better understand and minimize this effect.

NN SRC pairs have remarkably similar behavior in all nuclei [6] and understanding them is critical for understanding the short-distance and high-momentum behavior of nucleons. SRCs are pairs of nucleons with relative momenta p_{rel} much greater than typical mean-field nucleon momenta and center-of-mass p_{cm} momenta consistent with mean-field momenta. Almost all high-momentum nucleons in nuclei belong to an SRC pair [7]. When nucleons are at short relative distances, they experience a strong short-ranged interaction that generates these high relative momenta.

Experimental work has shown that about 20% of nucleons in medium to heavy nuclei belong to

SRC pairs and these pairs are predominantly neutron-proton pairs (at relative momenta of 300 to 600 MeV/c) [6–17]. As nucleons are composite objects, their internal structure (quark distributions) may be modified when the distance between the nucleons is smaller than their radii. In this way, the study of SRCs can give us information about bound nucleons and nuclear structure.

The study of SRCs is the subject of much experimental and theoretical work, as well as phenomenological applications to other areas of physics. A detailed overview of SRC physics is found in Ref. [6] and a theory-oriented description is in Ref. [8]. The following discussion will focus on the most recent results with their implications for $A = 3$ nuclei.

2.1 Few-body nuclear structure

Light nuclei are ideal for studying the nuclear system. In particular, $A = 3$ nuclei (mirror nuclei ${}^3\text{He}$ and ${}^3\text{H}$) play a unique role in nuclear structure studies. This system is complex enough to include some fundamental nuclear environment effects but simple enough that its ground state can still be exactly calculable. As will be detailed below, measurements on both ${}^3\text{He}$ and ${}^3\text{H}$ tightly constrain the reaction mechanism and NN interaction. Theory must be able to explain the data on both nuclei, and the combination of measurements on both is necessary to adequately account for the non-QE contributions. Consequently, the absolute cross section measurement on the $A = 3$ system can be used as a test for nuclear theory calculations.

The momentum distributions of $A = 3$ nuclei uniquely benchmark modern nuclear theory. In the QE limit with no re-scattering effects, the initial momentum of the probed nucleon (in this case, proton) is measured as p_{miss} . The simultaneous measurements of both ${}^3\text{He}$ and ${}^3\text{H}$ cross sections tightly constrain the contribution of non-QE reactions to our measurement, thus improving the purity of p_{miss} as it relates to the proton’s initial momentum. By measuring both ${}^3\text{He}$ and ${}^3\text{H}$, we improve our sensitivity to access the ground states.

As in the Hall A tritium measurements, we will measure absolute cross sections of $(e, e'p)$. We use various NN interaction models to predict the momentum distributions. Two primary momentum distributions are those from CDBonn-TMD and AV18+UIX as shown in Fig. 1 as a function of the proton momentum. We do not include predictions from Chiral Effective Field Theories as they are not valid for the high proton momentum (and small nucleon separation).

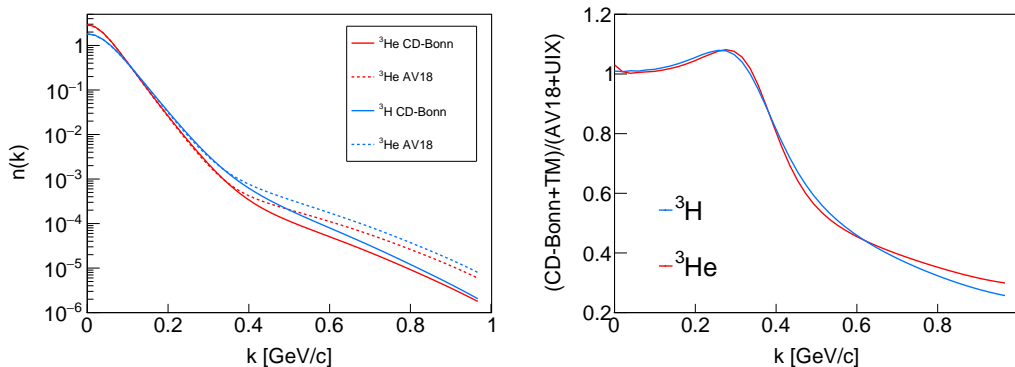


Figure 1: Left: The momentum distributions for ${}^3\text{He}$ and ${}^3\text{H}$ are shown for CD-Bonn+TM and AV18+UIX as a function of the proton momentum. Right: The ratio of ${}^3\text{He}$ and ${}^3\text{H}$ proton momentum distributions are shown using the CD-Bonn+TM potential relative to the AV18+UIX potential using the calculation in Ref. [18].

The right side of Fig. 1 shows the ratio of the ${}^3\text{He}$ and ${}^3\text{H}$ proton momentum distributions obtained using the CD-Bonn+TM potential relative to that obtaining using the AV18+UIX potential calculation in Ref. [18]. The different momentum distributions for ${}^3\text{He}$ and ${}^3\text{H}$ agree at low p , where

the NN potentials are well constrained by NN scattering. At larger p , where the NN potentials are not well constrained and where pion degrees of freedom make it harder to calculate NN potentials, these distributions begin to diverge.

The recent Hall A measurements measured the absolute cross section of ${}^3\text{H}$ and ${}^3\text{He}$ [19, 20] and compared the cross sections with state-of-the-art ab-initio calculations. The results are shown in Fig. 2.

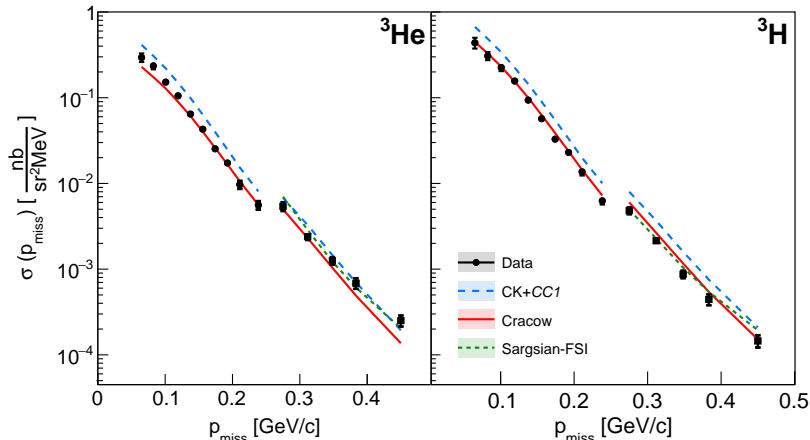


Figure 2: Absolute cross section as a function of p_{miss} for ${}^3\text{He}$ (left) and ${}^3\text{H}$ (right). The different sets of data points, depicted by black circles and squares, correspond to the cross sections measured in the low- p_{miss} and high- p_{miss} kinematical settings, respectively. The lines correspond to cross sections calculated from different theoretical models: Cracow (solid red), CK+CC1 (dashed blue) and Sargsian-FSI (dotted green, $p_{\text{miss}} > 250 \text{ MeV}/c$ only). The different kinematical settings have different average elementary electron-nucleon cross-sections and therefore have a different overall scale for both data and calculations.

These cross section measurements were taken at large momentum transfer ($\langle Q^2 \rangle \approx 1.9 \text{ (GeV}/c)^2$) and $x_B > 1$ kinematics, which minimizes contributions from MECs and ICs. A further requirement on the angle between momentum transfer and the missing momentum, $\theta_{p_{\text{miss}}q} < 40^\circ$, reduced the effects of FSIs. Thus, the measured cross sections were relatively sensitive to QE scattering from single nucleons. The data covered missing momenta $40 \leq p_{\text{miss}} \leq 500 \text{ MeV}/c$. The ratio of the measured to calculated cross sections is shown in Fig. 3 [20].

The data and ab initio PWIA calculations by the Cracow Group [26, 27] (which include the continuum interaction between the two unstruck nucleons, but not the rescattering of the struck nucleon) agreed to within about 20% for ${}^3\text{H}$ for the full p_{miss} range. The difference between data and calculation was within about 20% also for ${}^3\text{He}$ up to p_{miss} of 350 MeV/c . This validates the choice of kinematics and shows that the Hall A measurements have significantly reduced the effects of nucleon re-scattering, so that the measured cross sections are sensitive to the underlying ground state distributions.

Fig 4 left shows the ratios of the measured cross sections to the calculation of Sargsian that includes rescattering of the leading nucleon. Including the effects of re-scattering of the outgoing nucleon improves the agreement between data and calculations at $p_{\text{miss}} > 250 \text{ MeV}/c$. The diverging trend of this ratio for the two nuclei at higher p_{miss} is possibly the result of single charge-exchange (SCX) re-scattering (e.g., $(e, e'n)$ neutron knockout followed by a (n, p) charge exchange reaction) which could increase the ${}^3\text{He}(e, e'p)$ cross section and decrease the ${}^3\text{H}(e, e'p)$ cross section.

The isoscalar sum of ${}^3\text{He}$ plus ${}^3\text{H}$ (see Fig. 4) [20] should be largely insensitive to SCX. Fig. 4 right shows the data to theory ratio for the isoscalar sum of the $A = 3$ nuclei. Isoscalar data and

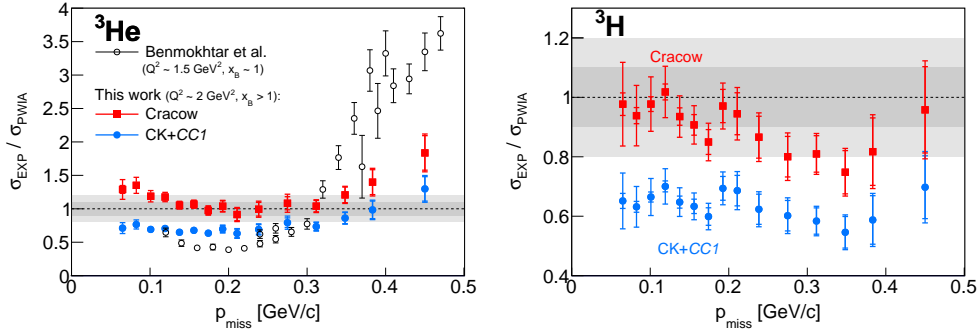


Figure 3: The ratio of the experimental cross section to different PWIA calculations plotted versus p_{miss} for ${}^3\text{He}(e, e'p)$ (left) and ${}^3\text{H}(e, e'p)$ (right). Red squares show the ratio to the Cracow calculation while blue circles show the ratio to the Ciofi-Kaptari spectral-function-based calculations (CK+CC1). Open symbols show the ${}^3\text{He}(e, e'p)$ data of Ref. [21], taken at lower Q^2 and $x \sim 1$ kinematics, compared with the PWIA calculations of Ref. [22–25]. The inner and outer bars show the statistical and statistical plus systematic uncertainties, respectively. The shaded regions show 10% and 20% agreement intervals [20].

theory agree to within the uncertainty of the data. This validates current models of the ground state of $A = 3$ nuclei up to very high initial nucleon momentum of 500 MeV/c.

Fig. 5 shows the ratio of ${}^3\text{He}$ and ${}^3\text{H}$ cross sections which should equal the ratio of the momentum distributions. In the simplest picture, the ratio of the number of protons in ${}^3\text{He}$ to ${}^3\text{H}$ should equal 2 at low momentum, due to simple nucleon counting, and decrease to 1 at high momentum, due to simple np SRC pair counting. The ratio at low momentum is larger than 2, due to a shift of more low-momentum protons in ${}^3\text{H}$ to high momentum caused by SRC pairing. This can be seen in the ratio of momentum distributions plotted in Fig. 5. The ratio of measured ${}^3\text{He}(e, e'p)$ to ${}^3\text{H}(e, e'p)$ cross sections [19] follows the calculated ratio of momentum distributions from $p_{miss} = 50$ to 250 MeV/c, but then is greater than that ratio by about 20–50% at larger p_{miss} . This is probably due to the SCX effects discussed above. Our proposed measurement will extend the measured p_{miss} spectra from the maximum of 0.5 GeV/c in the Hall A experiment to 1 GeV/c. We will also obtain high statistics over a range of angles that will enable detailed studies of the kinematic dependencies of the measurement and various FSIs.

This proposal will improve on the Hall A experiment in several ways. The CLAS12 detector accesses significantly larger solid angle than the Hall A spectrometers. This substantial improvement in solid angle more than compensates for the decreased luminosity compared to the Hall A experiments and will dramatically improve both the statistical uncertainties and the range of p_{miss} covered. It will also cover a wide range of kinematics (including a wide range in both θ_{rq} , x_B) and will include studies of deuterium that will allow us to explore the effects of contributions from other reaction mechanisms in order minimize their effects.

2.2 Asymmetric Nuclei

We previously re-analyzed CLAS data to extract the double ratio of the high-momentum fraction from different nuclei to ${}^{12}\text{C}$ for both the proton and the neutron to show that the proton is more correlated in neutron-rich nuclei [28]. This suggests that the minority nucleons (i.e., the protons) move faster than the majority nucleons (i.e., the neutrons) in neutron-rich nuclei, see Fig. 6. This result is opposite the simple expectation from a simple Fermi gas or mean-field nucleus.

This result was further tested by measuring the ratio of inclusive (e, e') cross sections of ${}^{48}\text{Ca}$ to ${}^{40}\text{Ca}$ in Hall A [29]. This measurement tests the effect of adding eight neutrons on the high momentum nucleons in Ca. The measured ${}^{48}\text{Ca}/{}^{40}\text{Ca}$ cross section ratio of about 1.17 shows that increasing

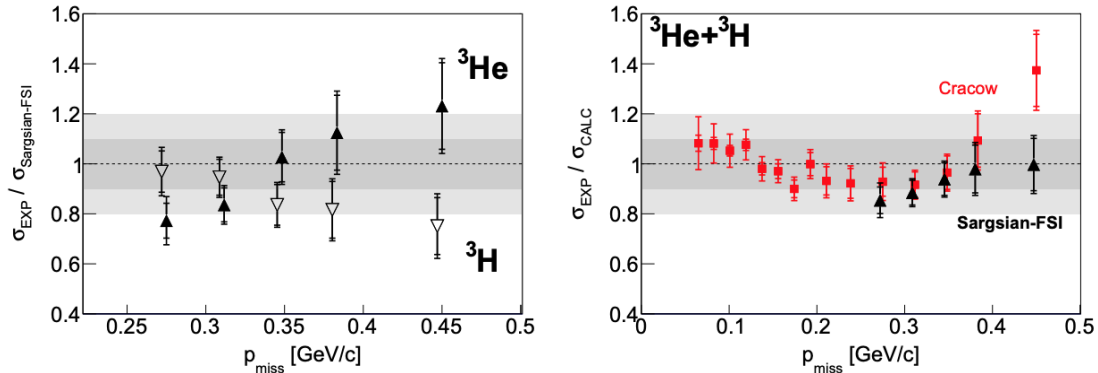


Figure 4: Left: The ratio of the experimental cross sections to the calculation of Sargsian that includes FSI of the leading nucleon for ${}^3\text{He}$ (filled upright triangles) and ${}^3\text{H}$ (open inverted triangles). Right: the ratio of the measured total ${}^3\text{He}+{}^3\text{H}$ cross section to the Cracow PWIA calculation (red squares) and the Sargsian calculation that includes FSI (black triangles). The inner and outer bars show the statistical and statistical plus systematic uncertainties respectively. On both panels the shaded regions show 10% and 20% agreement intervals.

the number of neutrons increases the fraction of high-momentum nucleons and thus increases the number of correlated pairs. This is consistent with the observation of Ref. [28], but because it is an inclusive measurement, we can not separate the proton and neutron contributions. The upcoming CaFe experiment [30] in Hall C will measure $(e, e'p)$ on ${}^{40}\text{Ca}$ and ${}^{48}\text{Ca}$ to answer the questions: 1) Does ${}^{48}\text{Ca}$ have more protons in SRCs compared to ${}^{40}\text{Ca}$? 2) What is the high-momentum fraction of protons in ${}^{48}\text{Ca}$?

All of these studies focus on medium and heavy asymmetric nuclei. It will be interesting to extend these studies to light asymmetric nuclei, and the most asymmetric stable light nuclei are ${}^3\text{H}$ ($N/Z = 2$) and ${}^3\text{He}$ ($N/Z = 0.5$). Particularly, these nuclei will test theory and our understanding of the observation we have made in the heavier nuclei. In this proposal, we will extract the high-momentum fraction for both protons and neutrons for ${}^3\text{H}$ and ${}^3\text{He}$ and compare them to the results obtained from heavier asymmetric nuclei.

2.3 Short range correlations

Studies of the short-ranged structure of nucleons in the nucleus have produced many fascinating results (see Ref. [6] and references therein). Per-nucleon ratios of inclusive electron scattering cross sections indicate that all nuclei have similar momentum distributions for $p_i \geq 275 \pm 25$ MeV/c and that this is due to the effects of NN SRC pairs. Measurements on ${}^{12}\text{C}$ and ${}^4\text{He}$ using both the $(e, e'pN)$ and $(p, 2pn)$ reactions show that knock-out of a high-initial-momentum ($p_i \geq 300$ MeV/c) proton from the nucleus almost always results in the emission of its correlated partner nucleon and that nucleon is almost always a neutron (for $300 \leq p_p \leq 600$ MeV/c). This indicates that almost all of these high-momentum nucleons belong to an SRC pair and that these pairs are predominantly pn pairs. These results were confirmed for heavier nuclei using data from CLAS [12, 28, 31]. These SRC pairs have a center-of-mass momentum distribution that is consistent with adding the momenta of two mean-field nucleons [32], and the probability of finding an SRC pair in a nucleus is proportional to the probability that two nucleons are in a node-less relative S -state [33]. This indicates that SRC pairs are momentary fluctuations of two short-distance nucleons into a short-lived high-relative momentum state.

More recently, measurements of $(e, e'p)$, $(e, e'pp)$, and $(e, e'pn)$ up to much higher nucleon mo-

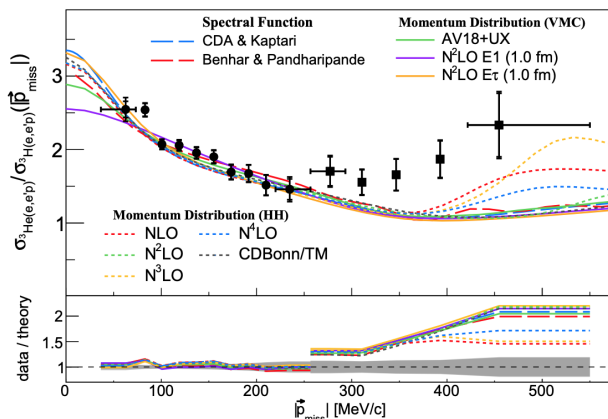


Figure 5: The measured ${}^3\text{He}$ to ${}^3\text{H}$ cross-section ratio, $\sigma_{3\text{He}(e,e'p)}/\sigma_{3\text{H}(e,e'p)}(p_{\text{miss}})$, plotted vs. p_{miss} compared with different models of the corresponding momentum distribution ratio [19]. The filled circle and square markers correspond to the low and high p_{miss} settings, respectively. Uncertainties shown include both statistical and point-to-point systematical uncertainties. The overall normalization uncertainty of about 1.8% is not shown. Horizontal bars indicate the bin sizes and are shown for only the first and last points in each kinematical setting as all other points are equally spaced. The bottom panel shows the double ratio of data to different calculated momentum distribution ratios, with the grey band showing the data uncertainty. The theoretical calculations are done using different local and non-local interactions, as well as different techniques for solving the three-body problem.

momentum [34, 35] show a transition from $300 \leq p_i \leq 600$ MeV/c, where there are far more np than pp pairs, to $600 \leq p_i \leq 1000$ MeV/c, where the relative number of np and pp pairs is determined by simple counting (see Figs. 7 and 8). This shows the transition from a spin-dependent (tensor) NN interaction to a spin-independent (scalar) interaction at high momentum.

We can describe these SRC pairs using the newly developed generalized contact formalism (GCF). The GCF exploits the scale separation between the strong interaction between the nucleons in an SRC pair and the pair's weaker interaction with its surroundings [32, 36, 37]. Using this scale separation, the two-nucleon density in either coordinate or momentum space (*i.e.*, the probability of finding two nucleons with relative and c.m. momenta q and Q respectively, or with separation r and distance R from the nucleus c.m. [38]) can be expressed at small separation or high relative momentum as [37]:

$$\begin{aligned} \rho_{\alpha,NN}^A(R,r) &= C_{\alpha,NN}^A(R) \times |\varphi_{NN}^\alpha(r)|^2, \\ n_{\alpha,NN}^A(Q,q) &= \tilde{C}_{\alpha,NN}^A(Q) \times |\tilde{\varphi}_{NN}^\alpha(q)|^2, \end{aligned} \quad (1)$$

where A denotes the nucleus, NN the nucleon pair (pn , pp , nn), and α stands for the quantum state (spin 0 or 1). φ_{NN}^α are universal two-body wave functions, given by the zero-energy solution of the two-body Schrödinger equation, and $\tilde{\varphi}_{NN}^\alpha$ are their Fourier transforms. φ_{NN}^α are universal in the weak sense, *i.e.*, they are nucleus independent but not model independent. Nucleus-dependent “nuclear contact coefficients” are given by

$$\begin{aligned} C_{\alpha,NN}^A &\equiv \int d\mathbf{R} C_{\alpha,NN}^A(R), \\ \tilde{C}_{\alpha,NN}^A &\equiv \frac{1}{(2\pi)^3} \int d\mathbf{Q} \tilde{C}_{\alpha,NN}^A(Q), \end{aligned} \quad (2)$$

and define the number of NN -SRC pairs in nucleus A .

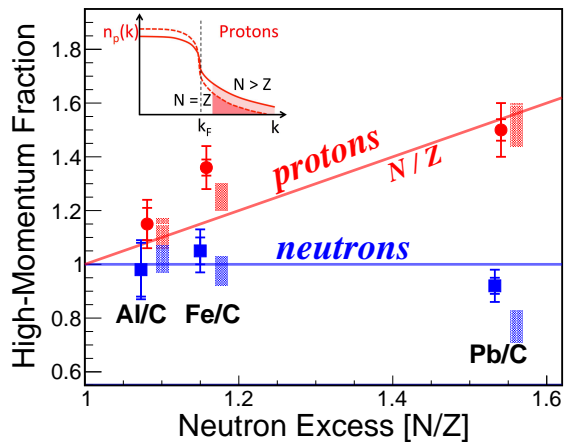


Figure 6: Relative high-momentum fractions for neutrons and protons. Red (blue) circles are double ratio of the number of $(e, e'p)$ high-momentum events to low-momentum proton (neutron) events for nucleus A relative to ^{12}C .

The GCF describes the measured momentum distributions of nuclei for $(e, e'p)$, $(e, e'pp)$ and $(e, e'pn)$ reactions remarkably well (see Figs. 7 and 8) and allows us to test the predictions of different NN interactions. By measuring $(e, e'p)$ and $(e, e'pp)$ up to $p_{miss} = 1000$ MeV/c we can test NN interactions in nuclei at remarkably short distances.

The NN interaction is a crucial input for calculations of nuclear structure and reactions as well as for other studies such as neutrino-less double beta decay and neutron stars. The NN force is not a fundamental force; it is due to the "leakage" of the strong interaction that binds quarks together to form the nucleon. Therefore NN interactions are described by effective theories. Current models have limited predictive power and are loosely constrained at short distance. Measuring nucleon momentum distributions in nuclei to high momenta allows us to constrain the NN interaction at previously unreachable short distances.

In Fig. 7, the measured ratio for $^{12}\text{C}(e, e'pp)/(e, e'p)$ is compared with GCF calculations using the phenomenological AV18 interaction, χEFT next-to-next-to-leading order (N2LO) interactions, and the scalar-only AV4' (lacking the tensor force) interaction. The AV18 potential agrees well with the data. The N2LO potentials include explicit cut offs at distances of 1 and 1.2 fm, corresponding to momentum cut offs at approximately 400-500 MeV/c and do not describe the data well above this cut off, as expected. The AV4' interaction is scalar-only (lacking the tensor force) and agrees with data in the scalar-dominated high-momentum region but fails in the tensor-dominated low-momentum region [34].

By extending these measurements to few-body nuclei we gain several advantages. Few-body nuclei already exhibit the same range of complex nuclear phenomena, including NN SRC pairs, as heavy nuclei, but they are far easier to calculate. There are many calculations of the ground state of $A = 3$ nuclei [2]. We can also compare these predictions to the more approximate GCF predictions, which can more easily incorporate many different NN interactions. The effects of FSI are much smaller in $(e, e'p)$ and $(e, e'pN)$ on few body nuclei, because there are many fewer nucleons to re-scatter from. There are calculations of nucleon re-scattering in $^3\text{He}(e, e'p)$ as discussed above. In addition, $A = 3$ nuclei have the added advantage of having both the largest and the smallest neutron to proton ratios of any "stable" nucleus with $A > 1$. This will allow us to test np and pp pairing hypotheses in the most extreme systems available.

We will measure the fraction of $(e, e'p)$ high- p_{miss} events with an associated second nucleon in order to study SRC pairing in $A = 3$ nuclei. If the struck proton belonged to an SRC pair, then its

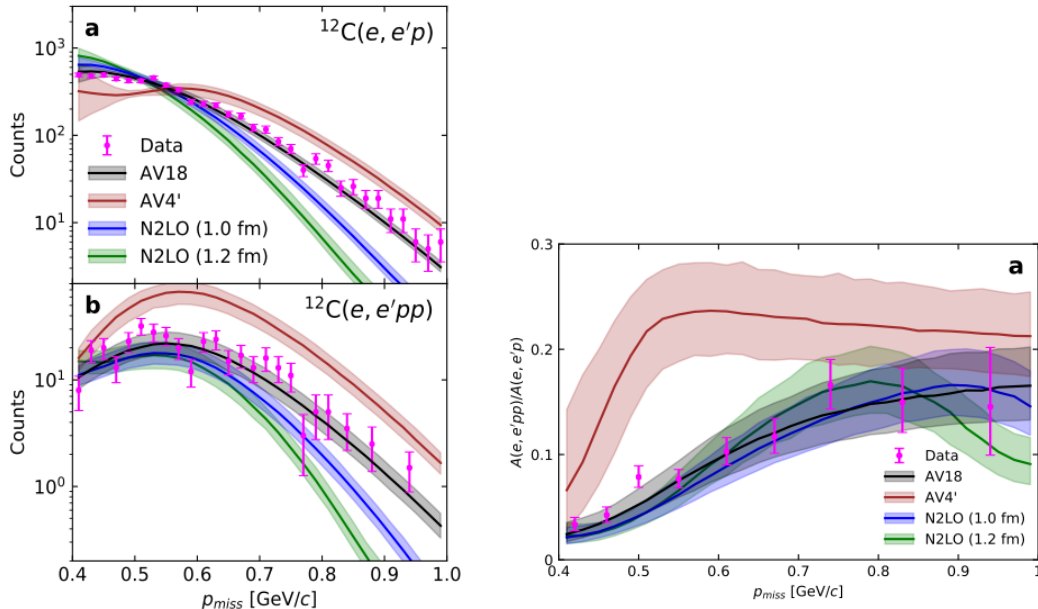


Figure 7: (left) Measured $^{12}\text{C}(e, e'p)$ (a) and $^{12}\text{C}(e, e'pp)$ (b) event yields shown as a function of the $(e, e'p)$ missing momentum compared with theoretical calculations based on the GCF framework, using different models of the NN interaction; (right) Measured $^{12}\text{C}(e, e'pp)/(e, e'p)$ event yields ratios shown as a function of the $(e, e'p)$ missing momentum compared with theoretical calculations based on the GCF framework using different models of the NN interaction [34].

partner nucleon should be ejected at high momentum and the 3rd, spectator nucleon, will have lower momentum $\vec{p}_3 = \vec{p}_{cm}$ where \vec{p}_{cm} is the center of mass momentum of the correlated pair. By looking at how the fraction of $(e, e'p)$ events with a correlated partner proton grows (and how the fraction with a correlated neutron partner decreases) as p_{miss} increases from 300 to 1000 MeV/c, we can study the transition from the tensor-dominated to the scalar-dominated part of the NN interaction. While the spin-1 pn pairs are dominant, this experiment will also let us study the 20-times less common spin-0 pp pairs. We will also explore other open questions, including the cm momentum distribution of pp and pn pairs, the relative momentum distribution of pp and pn pairs, and the relationship between the relative and cm momentum. All of these quantities are exactly calculable in $A = 3$ nuclei (for a given NN potential), unlike in heavier nuclei.

2.4 Neutron magnetic form factor

Electromagnetic form factors are fundamental, measurable quantities of nucleons describing their charge and current distributions as functions of Q^2 . The form factors are essential for constraining nucleon models, understanding spontaneous symmetry breaking in QCD, and constitute the zeroth moment of generalized parton distributions. Due to their importance in constraining our understanding of the nucleonic picture, the nucleon electromagnetic form factors are a key experimental objective of the JLab 12 GeV program with a goal being to measure the form factors over a large range of Q^2 with high-precision.

The lack of a free neutron target poses special challenges for the extraction of the form factors of the neutron. Neutron form factors must be extracted from quasi-elastic or elastic scattering measurements on deuterium or light nuclei, taking into account the effect of the nuclear wave function.

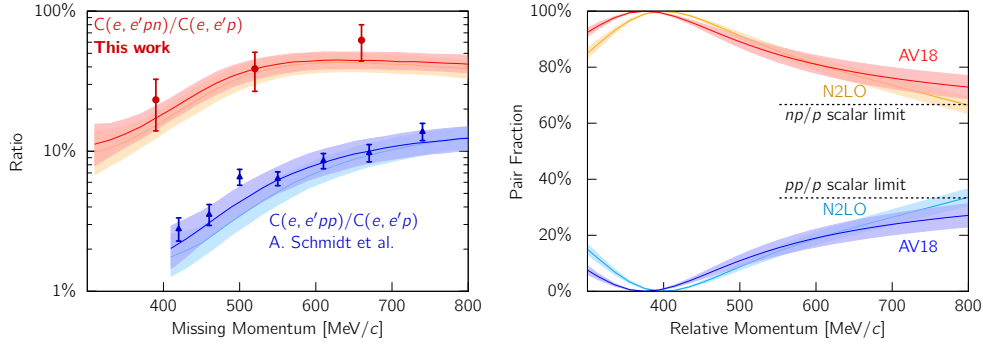


Figure 8: Left: The measured fractions of triple coincidence events ($C(e, e'pn)/C(e, e'p)$), compared with GCF predictions accounting for the variety of effects that influence the measurement (e.g. CLAS detector acceptance, efficiency, and resolution, FSIs including SCX, and the event-selection procedure) [35]. The $C(e, e'pp)/C(e, e'p)$ data (blue triangles) are taken from Ref. [34], while the $C(e, e'pn)/C(e, e'p)$ data (red circles) are from this work. Right: The GCF prediction for the ground-state fractions of pn and pp pairs as a function of pair relative momentum, calculated using the AV18 and N2LO NN interactions. The dashed line marks the scalar limit. The width of the GCF calculation bands shows their 68% confidence interval due to uncertainties on the model parameters.

Cross section measurements are essentially only sensitive to the neutron's magnetic form factor, G_M^n , since the neutron's electric form factor, G_E^n is much smaller by comparison, and can only be accessed through polarization asymmetries, sensitive to the G_E^n/G_M^n ratio.

Most previous determinations of G_M^n have been made from quasi-elastic scattering cross sections on deuterium. Systematic improvements can be made by tagging the struck nucleon, i.e., through the $d(e, e'n)p$ reaction, and further by simultaneously comparing to the $d(e, e'p)n$ reaction. The most precise determination of G_M^n was made over the Q^2 range from 1 to 5 [GeV/c]² using this technique at CLAS [39]. In the 12-GeV era, the CLAS-12 Run Group B recently collected data and intends to extract G_M^n to much larger Q^2 , and improve on the precision of earlier SLAC measurements [40]. The Super-Big Bite (SBS) program in Hall A intends to measure G_M^n out to $Q^2 = 13.5$ [GeV/c]².

Despite the push to higher Q^2 , there is still a troubling amount of uncertainty on G_M^n at low Q^2 . A selection of previously measured G_M^n values for $Q^2 < 5$ [GeV/c]² is shown in Fig. 9, relative to the standard dipole form factor, $G_D = (1 + Q^2/\Lambda^2)^{-2}$, where $\Lambda^2 = 0.71$ GeV²/c². Below 1 [GeV/c]², there is a discrepancy between older measurements [41, 42], and more recent measurements [43, 44] which found G_M^n to be slightly larger. A subsequent measurement in Hall A of the transverse beam-target asymmetry on polarized ³He found a smaller G_M^n [45]. This low- Q^2 discrepancy persists in theory, with Cloudy Bag Model calculations [46] favoring the larger G_M^n , while GPD-based calculations favor smaller values [47, 48]. New data are needed to help pin down G_M^n below 1 [GeV/c]², preferably with different systematic uncertainties.

The use of a tritium target presents a clear opportunity to make a defining low- Q^2 measurement of G_M^n . By measuring the inclusive quasi-elastic cross section for scattering from tritium relative to helium-3, one can extract G_M^n relative to the proton's magnetic form factor G_M^p , which is much better known. In the limit where nucleons are stationary, the ratio of G_M^n/G_M^p can be written

$$\left(\frac{G_M^n}{G_M^p}\right)^2 = \frac{\left(2\frac{\sigma_{3H}}{\sigma_{3He}} - 1\right) \left[1 + \frac{\epsilon}{\tau} \left(\frac{G_E^p}{G_M^p}\right)^2\right]}{2 + \frac{\sigma_{3H}}{\sigma_{3He}}}, \quad (3)$$

where $\tau \equiv Q^2/4m_N^2$, and ϵ is the virtual photon polarization parameter. The Fermi-motion of the nucleons in the $A = 3$ wave function complicate this simple relationship but do not diminish the

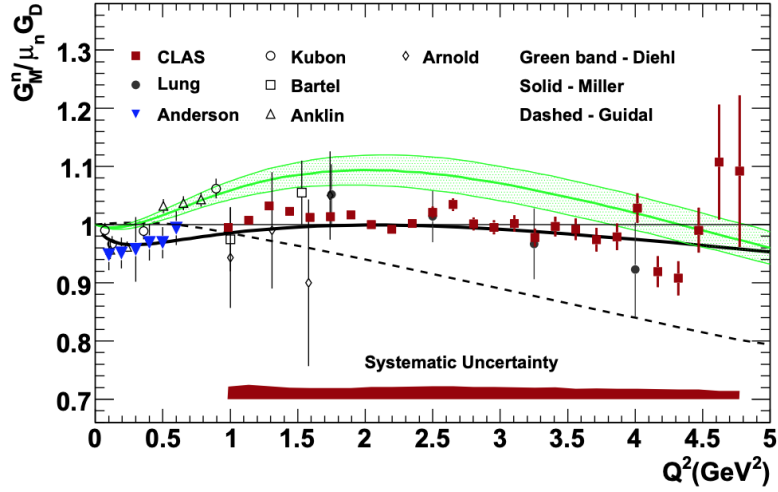


Figure 9: Select data for G_M^n at low Q^2 where the red points from CLAS cover the largest Q^2 range with good precision [39]. There exists significant contention between the data and model predictions at $Q^2 \leq 0.5[\text{GeV}/c]^2$.

sensitivity of the cross section ratio to G_M^n .

Extracting G_M^n by measuring ${}^3\text{H}(e, e')$ and ${}^3\text{He}(e, e')$ carries the huge advantage that no neutron detection is necessary. The inclusive measurements also count much faster than $(e, e'N)$ measurements. Furthermore, the sensitivity to the nuclear wave function is reduced by taking a cross section ratio. In fact, an extraction of G_M^n through this technique (at higher Q^2) was one of the main components of the 2018 Hall A experiment E12-11-112 is using this technique to measure G_M^n for $0.35 \leq Q^2 \leq 2.75$ (see Fig. 14). The CLAS measurement has the advantage of simultaneously measuring a higher density of points and a larger range of Q^2 , where high resolution is not critical.

This proposed experiment will measure the inclusive quasi-elastic cross section ratio of ${}^3\text{H}(e, e') / {}^3\text{He}(e, e')$ to make a high precision determination of G_M^n focusing on the region of $Q^2 < 1$ [GeV/c] 2 . This will shed valuable light on the discrepancy in previous low- Q^2 extractions of G_M^n with very different systematic uncertainties. The measurement will also complement the CLAS12 Run Group B and Hall A SBS measurements, allowing better constraint of the models of the nucleon form factors over the complete momentum transfer range.

3 Physics Goals

We will significantly impact our interpretation of models and constrain the theory of fundamental few-body nuclear physics by measuring cross sections with high statistics over a large kinematic range on both ${}^3\text{He}$ and ${}^3\text{H}$ targets. The isospin asymmetry of these two targets will also enable us to further extract information about the momentum distributions of minority and majority nucleons and the effects of SRC pairs. Through this measurement, we will specifically:

- benchmark few-body nuclear models,
- constrain the NN interaction and the nuclear wave function at high momentum,
- study scale separation in SRC pairs and pair formation mechanisms,

- determine the isospin of SRC pairs at different momenta,
- measure G_M^n at low and moderate Q^2

All of these goals are crucial for our understanding and interpretation of the dynamics in nuclei and will refine theory predictions for heavier nuclear systems. The inclusion of deuterium data will complement the measurements on ^3He and ^3H and are critical to the evaluation of non-QE contributions in the measured cross sections and observables. (Note that both the NN interaction and wave function are model dependent quantities. Unitary transformations can shift strength from the operator to the wave function and vice versa.)

3.1 NN interaction

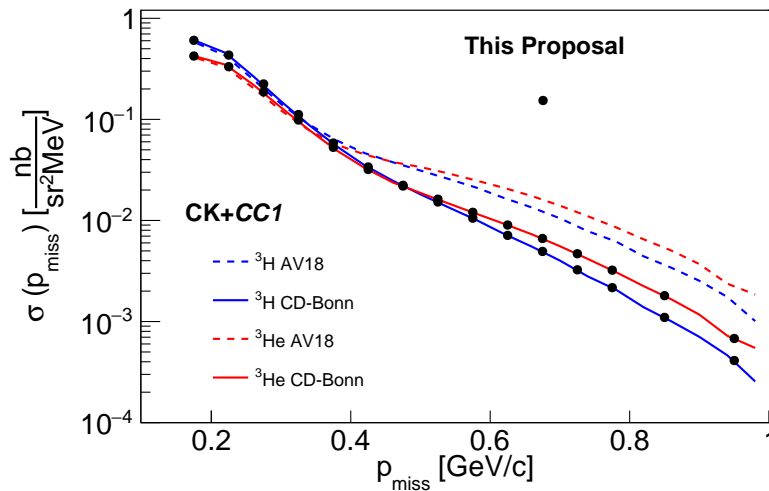


Figure 10: The factorized absolute cross section calculations using the Ciofi degli Atti and Kaptari spectral function together with the DeForest CC1 off-shell cross section are shown for both $^3\text{He}(e, e'p)$ and $^3\text{H}(e, e'p)$ for the AV18 and CD-Bonn NN interactions, separately. Our projected data points are shown by the black circles including our estimated statistical uncertainty and a 5% point-to-point systematic uncertainty (which are smaller than the data points).

We will measure QE absolute cross sections for $(e, e'p)$ on both ^3He and ^3H to constrain NN interaction models. We will measure over a wide range of x_B and Q^2 with p_{miss} up to ≈ 1 GeV/c. The $(e, e'p)$ cross sections will be compared to nuclear theory predictions using a wide variety of techniques and NN interactions in order to constrain the NN interaction at short distances.

Fig. 10 shows a factorized calculation of the absolute $^3\text{He}(e, e'p)$ and $^3\text{H}(e, e'p)$ cross sections using the ^3He spectral function of C. Ciofi degli Atti and L. P. Kaptari including the continuum interaction of the two spectator nucleons [49] and the σ_{cc1} electron off-shell nucleon cross section [5] using both the AV18 [50] and CD-Bonn [51] NN interactions. Due to the lack of ^3H proton spectral functions, we assume isospin symmetry and use the ^3He neutron spectral function. The expected uncertainties are smaller than the points.

Our cross section measurements will significantly extend the Hall A tritium measurements. The cross sections measured in Hall A along with our projected measurement in this proposal are shown in Fig. 11 and are compared to different PWIA calculations.

The proposed measurements we describe are shown as the black triangles in Fig. 11 along with the anticipated statistical and 5% point-to-point systematic uncertainties. The estimated statistical

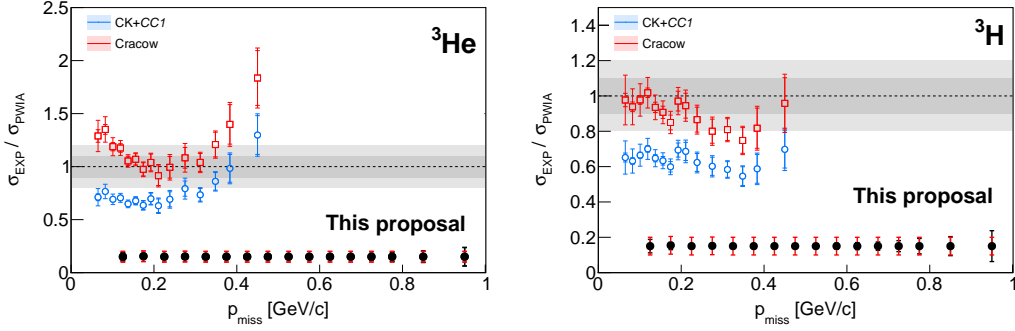


Figure 11: Left: The ${}^3\text{He}(e, e'p)$ experimental cross sections from Ref. [20] are shown with our proposed measurement (black triangles with statistical (black) and a 5% point-to-point systematic (red) uncertainty - the uncertainties are not combined). Right: The ${}^3\text{H}$ experimental cross sections from Ref. [20] are shown with our proposed measurement.

uncertainty is based on the proposed running in Table 2. We will make significant contributions for all p_{miss} up to 1 GeV/c.

The isoscalar sum of the ${}^3\text{He}$ and ${}^3\text{H}$ cross sections compared to PWIA calculations are shown in Fig. 12. This sum reduces the contributions from SCX and improves our sensitivity in evaluating the NN ground state. Furthermore, our measurement will be the first to evaluate calculations of these nuclei up to p_{miss} of 1 GeV/c.

3.2 Formation mechanisms and isospin dependence of SRC pairs

We will measure the $(e, e'pN)$ quasi-elastic reaction cross sections and the $(e, e'pN)/(e, e'p)$ ratios to understand SRC NN pairs in the simplest non-trivial system. For struck protons belonging to an SRC pair, the partner nucleon should be ejected at high momentum and the third, spectator nucleon, should have lower momentum $\vec{p}_3 = \vec{p}_{cm}$ where \vec{p}_{cm} is the center of mass momentum of the correlated pair. We will measure how the fraction of $(e, e'pp)/(e, e'p)$ events (the fraction of pp SRC pairs) changes with p_{miss} . This fraction should increase with increasing p_{miss} and show us the transition from the tensor to scalar-dominated regimes of the NN interaction. Similarly, the $(e, e'pn)/(e, e'p)$ fraction should decrease with p_{miss} .

As described in the Section 2, we can exploit the scale separation utilized by the GCF which describes the measured momentum distributions of nuclei for $(e, e'p)$, $(e, e'pp)$ and $(e, e'pn)$ reactions and makes predictions for different NN interactions. In this proposal, we will extract the contact terms for ${}^3\text{He}$ and ${}^3\text{H}$. Using the GCF, we can predict the $(e, e'pp)/(e, e'p)$ and $(e, e'pn)/(e, e'p)$ cross section ratios using different NN interactions as shown in Fig. 13.

The advantage of measuring $A = 3$ nuclei versus heavier nuclei as in many previous SRC observations is that the characteristics of these nuclei are exactly calculable. As shown in Fig. 13, we will extend the missing momentum range probing the NN interactions in nuclei at extremely short distances. The spin-1 pn are dominant at high p_{miss} , but this experiment will uniquely enable us to explore the 20-times less common spin-0 pp pairs. We can measure the center-of-mass momentum distributions of the pp and pn pairs, the relative momentum of the pp and pn pairs, and we can quantify the relationship between the relative and center-of-mass momentum. Importantly, all of these quantities are precisely calculable in $A = 3$ nuclei (for a given NN potential).

3.3 Neutron magnetic form factor, G_M^n

This experiment will measure G_M^n at low ($Q^2 < 1$ [GeV/c] 2) and moderate-range Q^2 . This measurement will use inclusive electron scattering from ${}^3\text{H}$ and ${}^3\text{He}$ targets at 2.2 and 6.6 GeV electron

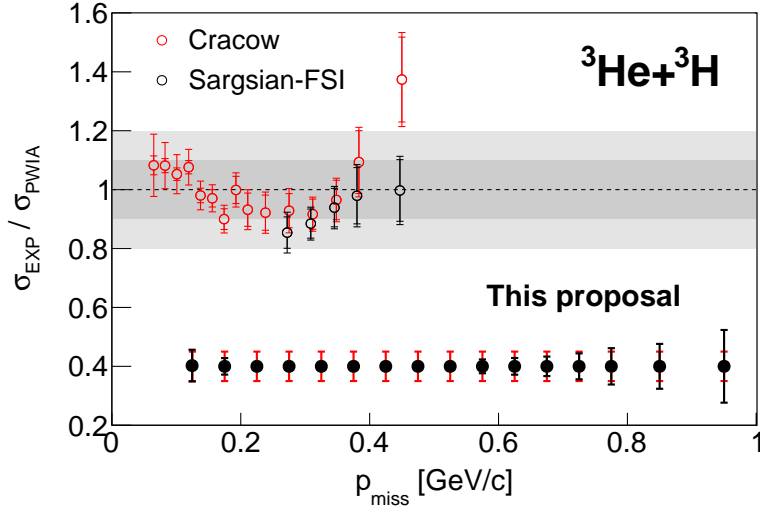


Figure 12: The ratio of the measured total ${}^3\text{He}+{}^3\text{H}$ cross sections relative to the Cracow PWIA and the Sargsian calculation that include FSI described in Ref. [20]. The projection of our measurement is shown by the black solid points where black error bar and red error bars are statistical and a 5% point-to-point systematic uncertainty, respectively.

beam running. For the run period proposed in Table 2, we anticipate the statistics shown in Fig. 14.

Fig. 14 shows the anticipated kinematic coverage and statistical uncertainty of the proposed experiment's extraction of G_M^n . In only one day of running on each target at 2.2 GeV, the proposed experiment will be able to thoroughly cover the kinematic region of $Q^2 < 1$ [GeV/c] 2 , exactly where there are discrepancies between the measurement from Hall A [45] and previous measurements, and where GPD and cloudy-bag theory begin to diverge. In addition, running at 6.6 GeV will have Q^2 overlap with the 2.2 GeV data and will be able to extend the Q^2 coverage. Extracting G_M^n from inclusive quasi-elastic data much above $Q^2 = 2$ [GeV/c] 2 will become difficult because of the increasing inelastic background. However, this region will be well-covered by CLAS12's run group B and at higher Q^2 by the Super-Big Bite program (both experiments using traditional scattering on deuterium), and is, therefore, not the focus of this proposal. Our measurements will complement these other experiments.

4 Proposed Measurement I: Quasi-elastic

4.1 Reaction mechanisms and event selection

4.2 $A(e, e'p)$ formalism

Assuming factorization, the cross-section for electron-induced proton knockout from nuclei $A(e, e'p)$ can be written as:

$$\frac{d^6\sigma}{d\omega dE_{miss} d\Omega_e d\Omega_p} = K\sigma_{ep}S^D(E_{miss}, P_{miss}) \quad (4)$$

where Ω_e and Ω_p are the electron and proton solid angles, respectively. σ_{ep} is the cross-section for scattering an electron from a bound proton [5]. $S^D(E_{miss}, P_{miss})$ is the distorted spectral function. In the absence of final state interactions (FSI), S is the nuclear spectral function that defines the

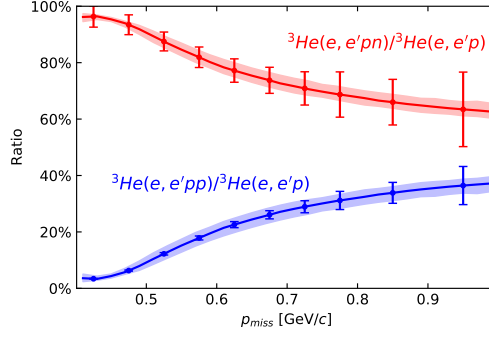


Figure 13: The GCF prediction for ${}^3\text{He}$ ratios of $(e, e'pp)/(e, e'p)$ and $(e, e'pn)/(e, e'p)$ using the AV18 interaction, $\sigma_{c.m.} = 100 \pm 20$ MeV, and the contacts from Ref. [52]. The points indicate the projected measurements of this proposal with anticipated statistical and 5% systematic uncertainty in the ratio. The ${}^3\text{H}(e, e'pn)/{}^3\text{H}(e, e'p)$ ratio (not shown) is expected to be approximately 1.

probability to find a nucleon in the nucleus with separation energy E_{miss} and momentum p_{miss} . The missing energy and missing momentum are:

$$E_{miss} = \omega - KE_p - KE_{A-1} \quad (5)$$

$$\vec{P}_{miss} = \vec{q} - \vec{P}_p \quad (6)$$

where KE_p and KE_{A-1} are the kinetic energies of the outgoing proton and residual nucleus. The momentum transfer $\vec{q} = \vec{P}_e - \vec{P}'_{e'}$, where \vec{P}_e and $\vec{P}'_{e'}$ are the initial and scattered electron momenta. $\omega = E - E_0$ is the energy transfer, and \vec{P}_p is the outgoing proton momentum. The kinematical factor, K , is:

$$K = \frac{E_p P_p}{(2\pi)^3} \quad (7)$$

4.2.1 Short range-correlated nucleon pairs

Here we discuss the desirable kinematics in selecting events where the beam electron scatters from a nucleon in an SRC pair, see Fig. 15.

There are many competing processes in the QE region that require us to fine tune our event selection criteria. These processes were mentioned in the Section 2 and include Meson Exchange Currents (MEC), Isobar Configurations (IC), and Final State Interactions (FSI), see Fig. 16. The amplitude of the MEC diagram decreases faster than the SRC amplitude by a factor of $1/Q^2$. We can reduce the contributions from MEC by choosing $Q^2 > 2$ [GeV/c] 2 . The contributions from both MEC and IC processes are also suppressed at $x_B > 1$.

The bottom center FSI diagram describes the FSI between the nucleons in the SRC pair. In this case, the FSI between the nucleons in the pair conserves its nucleonic composition and c.m. momentum, but changes p_{rel} . The bottom right describes the FSI of one of the nucleons with the resulting $A - 2$ system. At $Q^2 \geq 2$ GeV 2 the struck proton is ejected with enough momentum ($P_p > 1$ GeV/c) so that we can use the Glauber approximation to describe FSI. In addition, we can minimize the effects of FSI by selecting the angle between the recoil $A - 1$ system and \vec{q} , $\theta_{rq} < 40^\circ$. Table 1 shows the previously-used SRC event selection criteria.

The cuts on $\theta_{pq} < 25^\circ$ and $0.6 < |\vec{p}|/|\vec{q}| < 0.96$ select the "leading" proton, i.e., the proton that absorbed the virtual photon. The $x_B > 1.2$ or 1.4 cut and the $Q^2 \geq 2$ GeV 2 cut reduce the effects of MEC and IC. , The $m_{miss} < 1.1$ GeV cut eliminates events with an undetected pion (typically

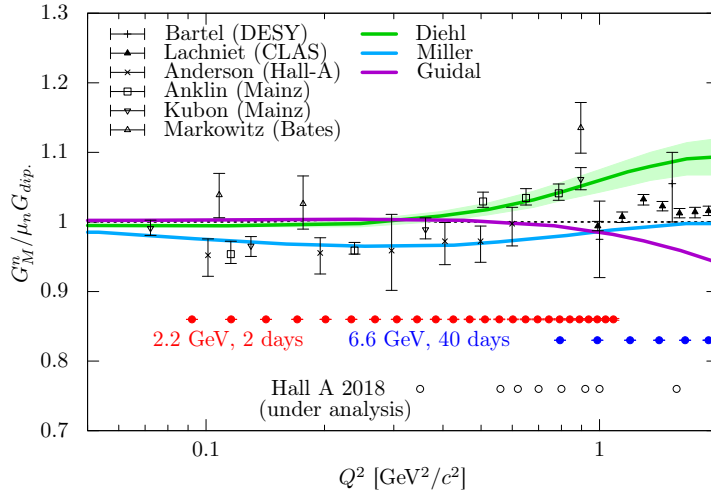


Figure 14: The anticipated kinematic coverage and statistical uncertainty of the determination of G_M^n compared to previous measurements [39, 41, 44, 45, 53, 54] and theory [46–48].

Table 1: Previously used $(e, e'p)$ and $(e, e'pN)$ SRC selection criteria. θ_{pq} is the angle between the knocked out proton and \vec{q} . $m_{miss}^2 = [(\vec{q}, \omega) + (\vec{0}, m_d) - (\vec{P}, E_p)]^2$ is the missing mass of the reaction assuming scattering off a stationary nucleon pair. m_d is the deuteron mass and E_p is the proton final energy from $E_p = \sqrt{\vec{P}^2 + m_p^2}$.

$x_B > 1.4$
$300 < \vec{P}_{miss} < 1000 \text{ MeV}/c$
$\theta_{pq} < 25^\circ$
$\theta_{rq} < 40^\circ$
$0.6 < \vec{p} / \vec{q} < 0.96$
$m_{miss} < 1.1 \text{ GeV}$

from IC or other resonant processes). The θ_{rq} cut reduces the effects of FSI. The p_{miss} cut selects protons from SRC pairs.

4.3 SRC observables

We propose to measure $A(e, e'p)$, and $A(e, e'pN)$ reactions on ^3He and ^3H using the CLAS12 spectrometer. We will use hydrogen elastic data to calibrate and normalize our data. We will also measure $d(e, e'p)$ to further understand contributions from FSIs and make comparisons. (The $A(e, e')$ reaction will be used to extract the ratio of σ_n/σ_p for obtaining the neutron magnetic form factor, G_M^n .)

For studying few-body nuclear structure and short range correlations, we will measure absolute cross sections for each target over $0 \leq p_{miss} \leq 1.1 \text{ GeV}/c$. We will measure the semi-inclusive $A(e, e'p)$ cross sections to extract nuclear momentum distribution for the $A = 3$ nuclei to compare to cross-section and momentum-distribution calculations. The isospin asymmetry between the $A = 3$ targets and the large kinematical coverage of the CLAS12 detector will enable us to study the reaction channels, evaluate non-QE contributions, and make strong comparisons with theoretical predictions.

We will also measure $(e, e'pN)$ cross sections and ratios, in order to measure the characteristics of the SRC pairs. These include their isospin/spin composition (pp , nn or pn pairs and either spin 1 or spin 0), their center-of-mass momentum distributions, and their relative momentum distributions.

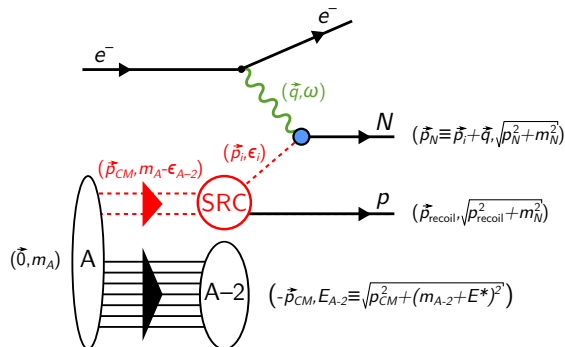


Figure 15: The diagram of an incoming beam electron emitting a virtual photon and interacting with a nucleon in an SRC pair in the nucleus. The original nucleus is described by A , and the recoiling $A - 2$ system is shown. The SRC pair yields the measured lead nucleon (proton in this proposal) along with the recoiling SRC-pair partner nucleon which may or may not be detected.

We also want to understand how their spin/isospin composition changes with missing momentum, in order to understand the tensor to scalar transition previously seen around 600 MeV/c [34].

4.4 Experimental setup and kinematical coverage

We will use the large-acceptance and open (i.e., electron only) trigger of the CLAS12 detector to measure inclusive and semi-inclusive hard scattering from ^3H , ^3He , and ^2H targets. While our proposal focuses on events where the leading nucleon is a proton, we will also be able to detect leading neutrons in the EC, as well as spectator correlated neutrons in the central neutron detector and BAND. The expected lead proton momentum and angle are shown in Fig. 17.

The majority of our $(e, e'p)$ and $(e, e'pN)$ events will be measured with an incident beam energy of 6.6 GeV. We used a simple phase-space generator to calculate the electron scattering acceptance. Rough CLAS12 fiducial cuts (determined by F.X. Girod from the standard GEMC CLAS12 geometry) were applied to the electron spectra. CLAS12 has a large kinematical acceptance as shown on the left in Fig. 18. In this proposal, we conservatively estimate rates and acceptances for scattered electrons at $\theta_e \geq 10^\circ$.

The event selection cuts of Table 1 dramatically increases the minimum accessible Q^2 (see Fig. 18right).

Fig. 19 shows the expected inclusive electron scattering rate as a function of Q^2 for the 2.2 GeV data.

The 2.2 GeV inclusive rates shown in Fig. 19 were compared to ^3He inclusive rates in the e2a experiment with the same beam energy where the minimum electron scattering angle was 20° . In CLAS12, the minimum scattering angle in Fig. 19 is cut off at 10° and significantly extends the reach to low Q^2 , a crucial region needed for precisely determining G_M^n .

4.5 Rate Estimation and beam time request

The rate estimation uses the measured $A(e, e'N)$ event rates on carbon from the CLAS6 EG2 experiment [12]. The EG2 experiment ran for 25 PAC days at an incident beam energy of 5 GeV on solid targets with a deuterium target cell in the beam, simultaneously. We doubled the rate to account for our single target cell. The effective usable gas-target luminosity of our proposed experiment is approximately the same as the luminosity of EG2 ($10^{34} \text{ cm}^{-2}\text{s}^{-1}$). Therefore, the carbon rates are scaled by a factor of two to account for the increased solid angle acceptance,

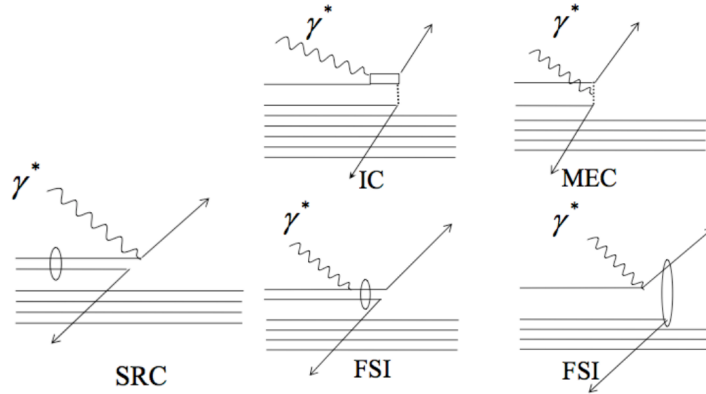


Figure 16: Shown are the diagrams of the relevant processes in the kinematic region where we expect to find SRC nucleon pairs. The true SRC signal is shown on the bottom far left. The MEC and IC diagrams are shown on the top. The bottom center FSI diagram describes the FSI between the nucleons in the SRC pair. The bottom right describes the FSI of the nucleons with the resulting $A - 2$ system.

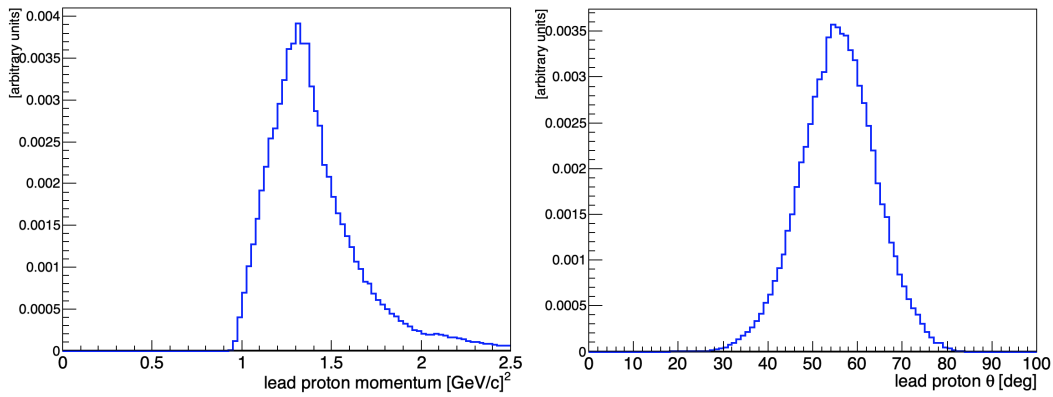


Figure 17: Left: The momentum of the leading proton. Right: The angle of the leading. These distributions include the lead proton cuts described in Table 1 with approximate electron fiducial cuts.

Mott cross-section (5 to 6.6 GeV beam energy), and recoil detection. Assuming $A^{-1/3}$ scaling (corresponding to the probability that a knocked out nucleon in a nucleus A escapes the nucleus where nucleons in carbon have a 40% chance to escape versus the nucleons in $A = 3$ that have a 70% chance to escape), the rates are increased by a factor of 1.6 from the $A = 12$ carbon nucleus to the $A = 3$ nuclei.

As a check, we used the $A = 3$ Cracow calculations [26,27] (used in the Hall A tritium study in Ref. [20]) to generate the total cross section for discrete kinematic points. We compared this cross section with the scaled measured $C(e, e'p)$ yields. The Cracow calculations give about $1/2 - 1/3$ as many events as the carbon data. This is roughly consistent with ratio of the AV18 extracted contact terms of carbon to the ${}^3\text{H}$ and ${}^3\text{He}$ nuclei which yields a ratio of approximately $7/18$ [55]. Therefore, we applied a conservative factor of $1/3$ scaling to the scaled $C(e, e'p)$ statistics.

The number of beam days per target is shown in Table 2. We request 20 days for high statistics running on each $A = 3$ target at 6.6 GeV. This should give us about 6000 $(e, e'pN)$ events each with a leading proton and a recoil proton or neutron, see Table 3. The $(e, e'pn)$ event rate for ${}^3\text{H}$

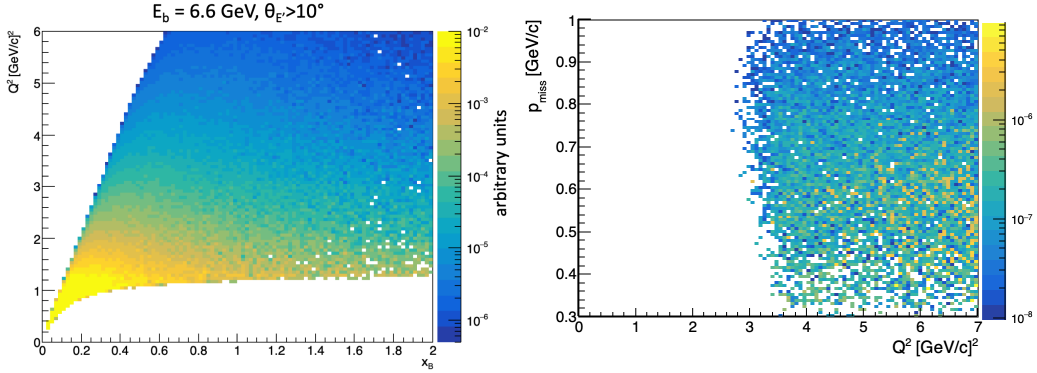


Figure 18: Left: The general phase space acceptance for electrons in the CLAS12 detector at minimum angles greater than 10° for an electron beam of 6.6 GeV. Right: The distribution of minimum accessible Q^2 for an incident 6.6 GeV electron beam for the selection criterion listed in Table 1. This distribution is generated using the GCF AV18 interaction and the z -axis units are arbitrary.

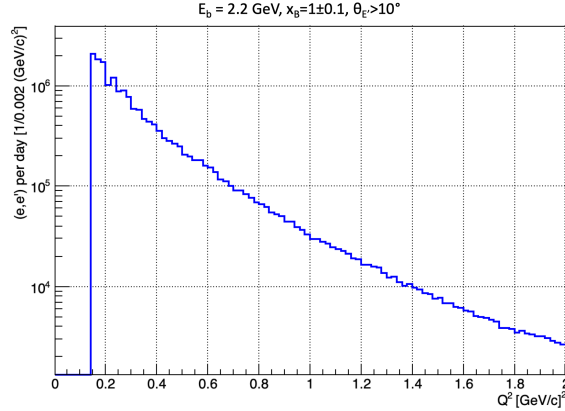


Figure 19: The inclusive rate is shown for a 2.2 GeV electron beam as a function of accessible Q^2 . The minimum angle here is 10° . The Q^2 range is truncated at $2 \text{ GeV}^2/c^2$ beyond which we will not extract G_M^n .

and ^3He should be similar at large p_{miss} . Deuterium has approximately half the number of SRC pairs compared to ^3H (and therefore, half of the statistics at high missing momentum for the same run time). We require deuterium to constrain FSIs in order to better calculate reactions on $A = 3$ nuclei. Deuterium having 25% statistics (compared to ^3H) in the high missing momentum regime is sufficient for this experiment. Therefore, we request 10 days of running on deuterium. We will use hydrogen to optimize our calibration and measure the absolute cross section for efficiency studies and systematic effects. Table 2 includes 1 day (3 shifts or 0.5 PAC days) of overhead for each target change.

The field will be in the electron out-bending configuration for the 2.2 GeV beam running and will be in the electron in-bending configuration for the 6.6 GeV beam energy run. We include one pass change from 2.2 GeV beam energy to 6.6 GeV beam energy that should take half of a shift.

For the $A(e, e'p)$ reaction specifically, we anticipate the statistics for the requested beam time in the high missing momentum regime as shown in Figs. 11 and 12, which will enable us to discern between various theoretical models. This experiment uniquely accesses this regime with high statistics

Table 2: Requested beam time per target, including calibration time and target change overhead.

Target:	¹ H	² H	³ He	³ H	Total
Measurement Days (6.6 GeV)	1	10	20	20	51
Calibration (inbending field)					1
Target Changes					2
Total at 6.6 GeV:					54
Measurement Days (2.2 GeV)	0.5	0	1	1	2.5
Calibration (outbending field)					1
Target Changes					2
Total at 2.2 GeV:					5.5
Total beam time requested:					59.5

Table 3: Expected number of counts for 2N knockout reactions for 20 beam days on each target ³He and ³H at 6.6 GeV beam energy. The reaction notation is that the first nucleon is the “leading” nucleon (i.e., a high-momentum nucleon that is emitted largely in the momentum transfer direction), and other nucleons are the recoil nucleons. We consider cases only where the leading nucleon is a proton.

Reaction	(<i>e, e'pp</i>)	(<i>e, e'pn</i>)
# events (6.6 GeV)	8k	6k

on these calculable nuclei.

As detailed in the next Section 5, for our expected luminosity on ³H of $2 \times 10^{34} \text{ cm}^{-2}\text{s}^{-1}$, we intend to run at a requested beam current of 110 nA. This configuration will not require rastered beam.

5 Target design

A new gas target system is proposed for this measurement. While a detailed conceptual design is not presented here, we propose that such a system should build on the experiences and lessons learned from the Hall A Tritium Target (HATT) which is described in detail in reference [56]. While this system would be unique, the same rigor that was applied to the Hall A system would also be applied in Hall B. The safety systems and subsystems for the proposed target are necessarily complex and can only be summarized in this proposal. This includes numerous engineered and administrative controls, only some of which are listed below.

- A minimum of three layers of containment and or confinement shall be employed at all times. This includes operations, installation/removal, shipping and handling, and storage.
- The cell shall be constructed in compliance (and indeed in excess of compliance) with JLAB pressure safety requirements, SRTE safety basis requirements, and applicable ASME Codes, namely ASME B31.3 and ASME BPVC VIII D1 and D2. Design safety factors for the cell shall exceed 10. This shall be verified by through destructive testing.
- Strict access controls shall be required for the Hall while the cell is installed. These include specific training, locked badge access to the Hall including truck ramp access, and procedures for entrance/exit of the Hall. These controls are partly to ensure that the Hall will be the third layer of confinement while the cell is installed.
- An extensive review process shall be employed, specifically:

- Technical and Peer reviews as required by EHSQ 6151 and supplement.
 - Review by Savannah River Tritium Enterprises and DOE-NNSA.
 - Multiple reviews by JLAB and outside Subject Matter Experts (SME) as part of the formal ERR process addressing all aspects of the system.
- Full Failure Mode Effects and Criticality Analysis (FMECA) shall be performed and reviewed by SMEs. All failure modes shall be addressed including complete failure of the containment/confinement system.
 - Examinations of materials, completed components, welds, mechanical fabrications, etc. shall be performed by qualified personnel in accordance with approved procedures.
 - Inspections verifying all appropriate examinations have been performed and documented by qualified personnel using correct procedures and calibrated/certified equipment.
 - Specific training and additional qualifications shall be required for all personnel accessing the Hall and performing any fabrication function.
 - A thorough review and site inspection by EHS and Physics Div SMEs ensuring all applicable safety systems are installed and are operating correctly shall be performed.

The proposed system would employ three sealed gas cells filled with 2H_2 , 3H_2 , and 3He . Given the limited space in CLAS12, a motion system is not possible, and the cells would need to be installed separately, marking three distinct run periods. The Hall B tritium target is expected to incorporate the same major components as the Hall A system which are listed below.

- Target Cell
- Exhaust system including stack
- Containment/confinement system including the scattering chamber and Hall B under strict access controls.
- Cryogenic cooling system

Some conceptual design work has been performed and is shown in the subsections below. Rate estimates reported elsewhere in this proposal are based, at least in part, on the thicknesses, materials, and geometries presented in this concept.

5.1 Tritium Containment and Confinement

The primary method for ensuring safe operations with tritium is to establish multi-layer containment and or confinement at all times. The proposed system would rely on a series of engineering and administrative controls to provide at least three layers of tritium confinement and/or containment during all phases of operation. Confinement as defined here would limit a possible tritium release to a controlled region were it would be collected and stacked (exhausted to the environment) in a safe manner. A summary of the three layers of containment/confinement are shown in the table below for each operational condition (configuration).

Configuration	Layer 1	Layer 2	Layer 3
Installation/Removal	Cell	Handling Hut and Scattering Chamber	Hall B
Shipping/Storage	Cell	Inner Containment Vessel	Outer Containment Vessel
Beam Operations	Cell	Scattering Chamber	Hall B

It is important to note that during beam operations, the Hall and scattering chamber must each be considered as one layer of the confinement system. This has implications for the design of the scattering chamber. It also requires that the exhaust system and access controls are designed to ensure that the Hall and chamber can indeed be considered layers of confinement.

5.2 Target Cell

A conceptual model of the cell is shown in Figures 20, 21, and 22. With the exception of the fill valve assembly, the cell is fabricated from ASTM B209 7075-T651 aluminum. This material has many distinct advantages, primarily, being nearly twice the strength and hardness of more common alloys (e.g. 6061). It has also undergone Jefferson Lab sponsored testing at Savannah River National Laboratory confirming suitability for tritium service at our operating conditions [57]. The proposed cell for the Hall B target allows full azimuthal angle acceptance and backward polar angle acceptance, with minimal loss of target length, to 120° . The azimuthal symmetry also greatly simplifies the design of the target cell making it much easier to fabricate than the HATT cell. The target cell is expected to be 12.7 mm in diameter and 25 cm long with a fill pressure of about 200 psi. Thus, the total amount of tritium would be about 1200 Ci. The thickness of the cell wall is 0.4 mm with the exception of the beam entrance and exit which are expected to be 0.25 mm. While these thicknesses are not optimal when considering the physics, they do provide a suitable level of safety both during beam operations and during the filling of the cell off site. Similar sealed gas cells were used in Hall A for the Tritium Family of experiments and performed at $22.5\mu A$ with acceptable density reduction [58]. Filling of the tritium cell is expected to be performed at Savannah River Site where overpressure protection requirements are substantially higher than the fill/operating pressure of the cell.

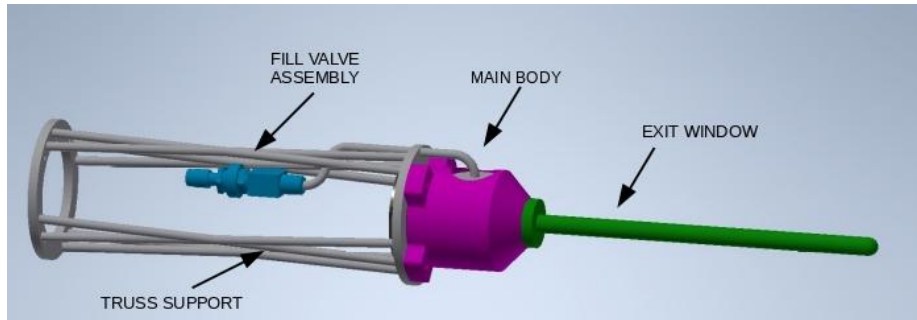


Figure 20: External side view of the conceptual design of the target cell as seen from the beam right side.

Hydrogen is known to permeate through most materials. A model was developed for the expected permeation of tritium from the HATT cell [59]. The expected operational loss of tritium from the cell is less than 0.8 Ci per year due mostly to permeation through the thin cell walls. This is similar to the loss observed in Hall A during operations. This loss, although small, would be collected by the pumping system and stacked.

The temperature of the cell wall should not exceed 170K for extended periods of time. This is a design requirement based on previous studies of hydrogen embrittlement in aluminum with an impinging electron beam [60]. In Hall A, the cooling system was supplied by 15K helium from the ESR. For practical reasons, a dedicated cooling system (similar to that of the Hall D cryogenic target) should be used for a Hall B target. A stand alone pulse-tube refrigerator system such as the CryoMech PT410 with a cold finger would simplify the design and provide operational reliability. The beam current necessary to complete the measurements is much less than $1\mu A$. The heat generated in the cell with this current would be less than 1 W, with the majority being generated in the entrance

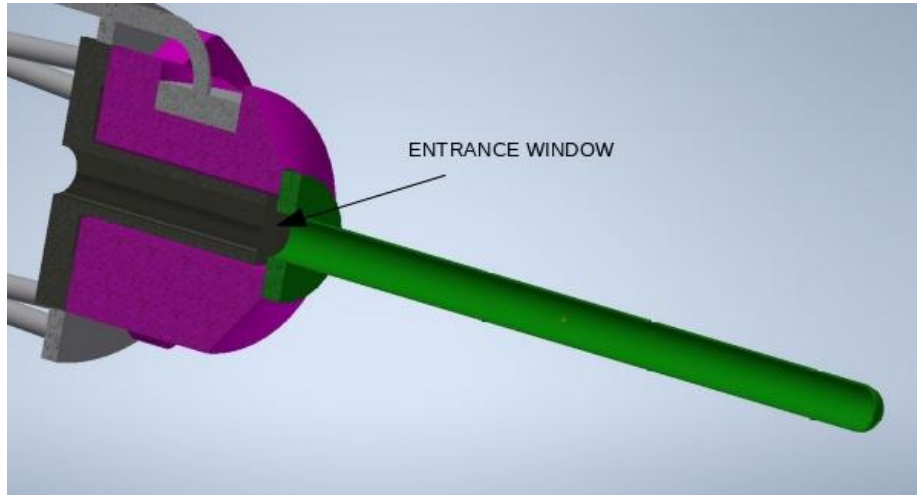


Figure 21: Section view of the conceptual design of the target cell.

and exit windows. A thermal model of the cell exit window (the component most affected by the heat load) has been developed assuming following conditions

- Beam current $1 \mu A$
- Beam spot size of 0.250 mm
- Cold sink operating temperature 40K
- Cold finger length 3 m
- Cold finger cross section 1 cm^2
- Model is run in steady state only

The model was developed using an ANSYS steady state thermal analysis. The results of this simulation are shown in Figures 23 and 24

5.3 Scattering Chamber and Vacuum System

Because the scattering chamber must be a layer of tritium confinement, it cannot be fabricated from materials that are significantly permeable to tritium. Thus, the foam chamber typically used in Hall B will have to be replaced. We propose a chamber fabricated from aluminum (ASTM B209 7075-T651) with geometry as shown in Figure 25. In this design, the part of the chamber surrounding the cell is cylindrical with a hemispherical head and has a diameter of 25 mm. Some details of the chamber geometry are shown in Figure 26. Calculations (in compliance with ASME Boiler and Pressure Vessel Code Sec VIII Div 1 and Div 2) show that a wall thickness of 0.4 mm will exceed a safety factor of 2 for buckling from the external pressure. The beam exit of the chamber (tip of the hemisphere) shall be thinned to 0.25 mm. The chamber must also be isolated from the upstream beam line via a 0.2 mm thick beryllium window. Additionally, the chamber volume must be large enough to contain a gas cell failure and still maintain a sub-atmospheric pressure. The vacuum in the chamber would be maintained by a series of mechanical and turbo pumps which would exhaust to the stack.

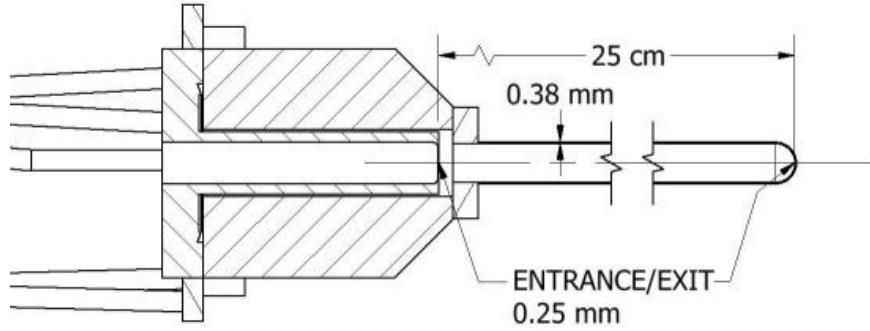


Figure 22: Detail side section view of the target cell with thickness and length. Note that the active region of the cell is 25 mm long.

5.4 Luminosities

It is important to consider that the aluminum walls of the target cell and scattering chamber in the proposed design are relatively much thicker than the nominal Hall B cryotarget configuration. The reasons for this have been discussed in the previous sections. A summary of the assumed thickness and luminosity for the tritium cell, both fluid and metallic components, is shown in Table 4. The fluids in the 2H_2 and 3He cells are expected to have fluid densities of 125% and 150% of the tritium cell. The entrance and exit windows (Al windows) for the cell and chamber have been combined into one thickness.

Material	Tritium	Al Windows	Be Window	Total
Length(g/cm ²)	0.085	0.21	0.037	0.33
Luminosity	3.54×10^{34}	8.42×10^{34}	1.54×10^{34}	1.35×10^{35}

Table 4: Assumed density and luminosity for each component. Note that the maximum luminosity of CLAS12 is 1.35×10^{35} nucleon/cm²/s

5.5 Exhaust System and Stack

A dedicated exhaust system and stack shall be constructed to remove tritium from Hall B similar to the system developed for Hall A. Calculations for tritium release resulting from a catastrophic cell failure were performed using HotSpot [61]. This is a DOE approved collection of atmospheric dispersion models which are designed for near-surface releases, short-range (less than 10 km) dispersion, and short-term (less than 24 hours) release durations in unobstructed terrain and simple meteorological conditions. These calculations, summarized in [56], indicate the exhaust stack must be at least 20 m above grade at the site boundary. (Note the the position of the Hall B stack would be less than 15 m from the current Hall A stack.) This ensures that any release will not cause an undue exposure to the public. The exhaust system shall be driven by a fan which pulls air through Hall B (maintaining a slight negative pressure) into the stack via one of the smoke removal ports. Thus, the exhaust system serves two purposes: tritium removal and smoke removal. This system must also stack the exhaust from the vacuum pumps connected to the scattering chamber and downstream beam line. These subsystems are necessary to ensure at least three layers of containment or

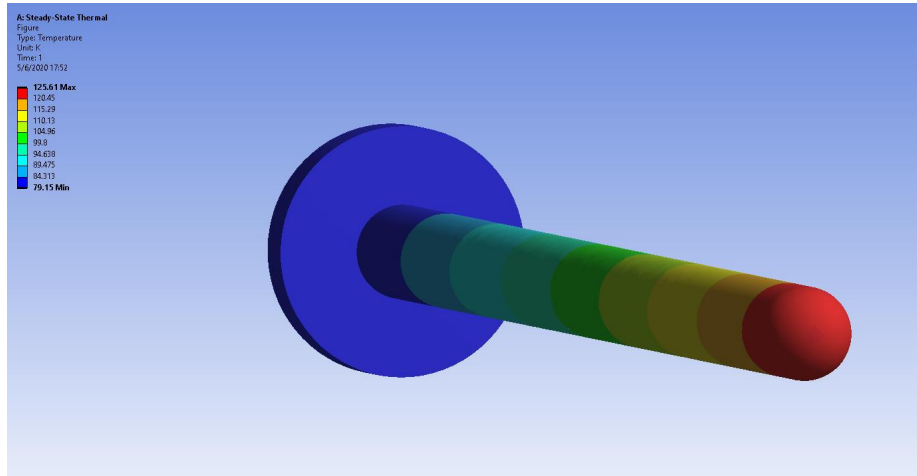


Figure 23: Temperature profile of the aluminum exit window under the conditions listed above. The maximum temperature (red) is 126K and minimum (blue) is 80K

confinement as discussed previously.

5.6 Transportation and Storage

The HATT cell was filled at Savannah River Site and shipped to Jefferson Lab in the Bulk Tritium Shipping Package (BTSP) as a miscellaneous tritium vessel (MTV). The same mechanism is expected to be employed for filling and shipping a similar cell for the Hall B target. An expert team from SRS traveled to Jefferson Lab to assist in the unpackaging and packaging of the cell to and from the BTSP. The Hall B tritium cell would be filled and transported in the same manner. The storage system employed in Hall A can also be used in Hall B. This system allowed the target cell to be removed from the beam line for longer term storage (up to a few months) during accelerator down periods. It also simplifies packaging and unpackaging operations associated with shipment of the cell.

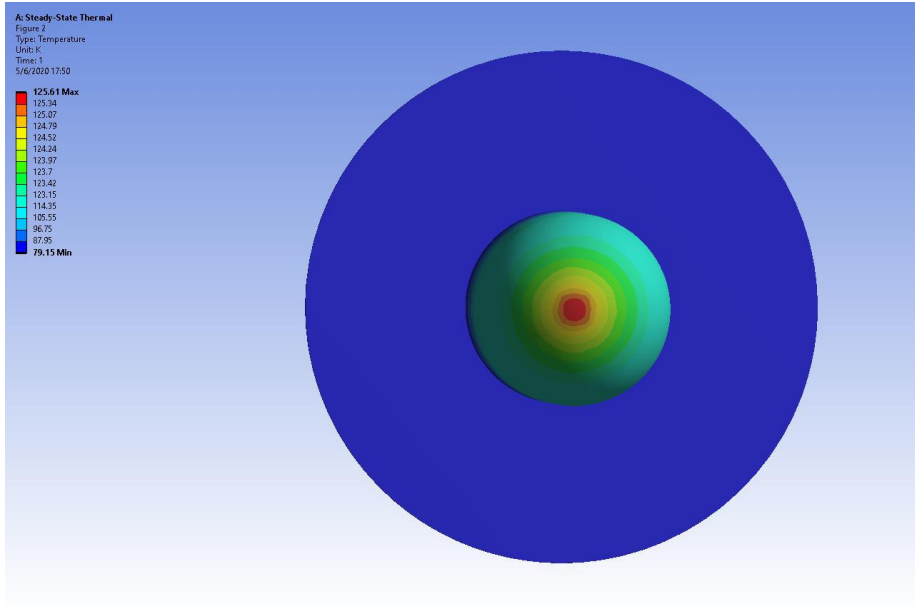


Figure 24: Temperature profile of the exit window tip under the beam conditions listed above. Note that the beam passes through the dark red area in a uniform 0.250 mm spot size and that the temperature scale in this figure has been logarithmically inflated near the tip.

5.7 Conclusion

We conclude that a tritium target similar to the system developed for use in Hall A could be similarly employed in Hall B. While an exhaust system would need to be developed, there are many other aspects of the proposed Hall B system that would make the design and fabrication more simple. The proposed target cell would be installed on a dedicated insertion cart for the duration of the tritium run. Therefore, no motion system is required. Further, with the use of a dedicated cryo-cooler and lower beam current the cell and heat sink design are also simplified. Based on a similar analysis performed for the HATT, a release, in a controlled fashion through the stack or through the truck ramp, of the full load of tritium contained in the cell is not expected to pose a significant risk to personnel on site or to the public.

Because the Hall A target and the proposed Hall B target are very similar, the budget for each system is also expected to be similar. Some expenses that were incurred in the Hall A project, such as the tritium exposure study of aluminum 7075 will not have to be repeated.

6 Relation to other approved 12 GeV measurements

There is no experiment to date that probes both ^3He and ^3H across the full quasi-elastic kinematical regime. While the Hall A tritium experiments showed that we can learn much from these isospin asymmetric targets, our fundamental understanding of the NN wave function will only be fully constrained from studies on both targets with a more thorough evaluation of the non-QE reaction mechanisms. Including deuterium will improve our understanding of FSIs in the limit of a two-body system. These studies will be naturally accessible from the large acceptance of the CLAS12 detector and will yield new measurements to higher p_{miss} where different momentum distribution models can be tested. Our measurements will support the interpretation of the Hall A ^3H spectrometer measurements and will improve our interpretation of future experiments on heavier nuclei such as

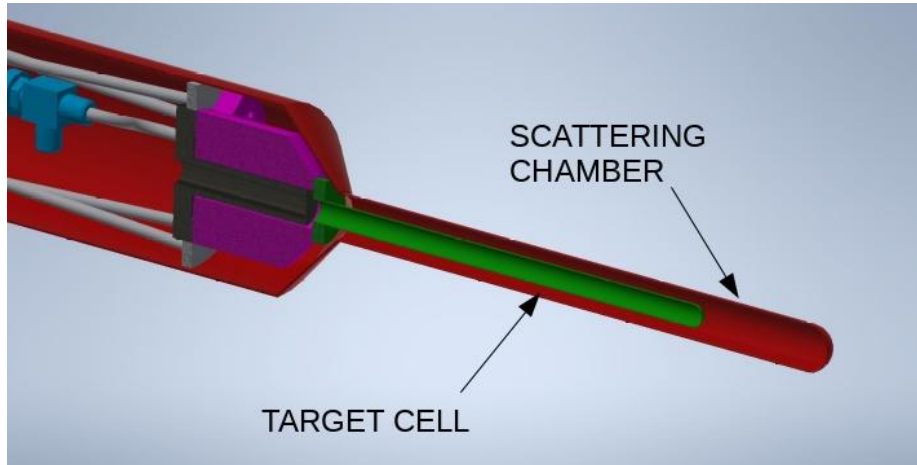


Figure 25: Section view of the target cell/chamber assembly

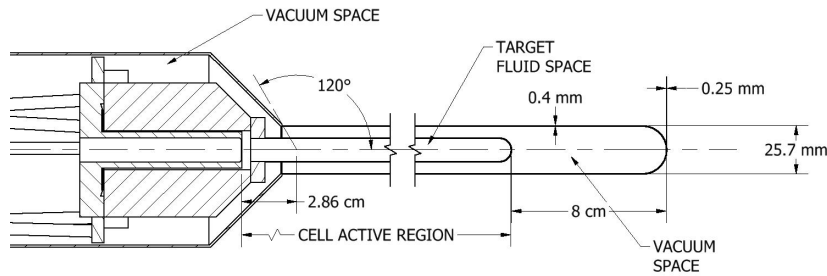


Figure 26: Detail section view cell/chamber assembly with some dimensional detail. Note that for 120° the effective length of the target is shortened by less than 3 cm.

the study of SRCs using CLAS12 in Run Group M.

Additionally, our experiment will also measure G_M^n by comparing the inclusive scattering cross sections from ^3He and ^3H , covering the crucial low Q^2 regime with different systematics than measurements from deuterium. These measurements will be a significant improvement on the previous measurements of G_M^n at low Q^2 and will support the overall understanding of G_M^n which will be an important interpretation to the recent Run Group B measurement and future SBS measurement.

References

- [1] O. Hen et al. LOI: Next Generation Tritium Experiments in CLAS12. Letter of Intent to Jefferson Lab PAC 47, 2019.
- [2] William P. Ford, Sabine Jeschonnek, and J. W. Van Orden. Momentum distributions for $^2\text{H}(e, e'p)$. *Physical Review C*, 90(6), Dec 2014.

- [3] C. Marchand, M. Bernheim, P. C. Dunn, A. Gérard, J. M. Laget, A. Magnon, J. Morgenstern, J. Mougey, J. Picard, D. Reffay-Pikeroen, S. Turck-Chieze, P. Vernin, M. K. Brussel, G. P. Capitani, E. De Sanctis, S. Frullani, and F. Garibaldi. High proton momenta and nucleon-nucleon correlations in the reaction ${}^3\text{He}(e, e'p)$. *Phys. Rev. Lett.*, 60:1703–1706, Apr 1988.
- [4] Frank Vera and Misak M. Sargsian. Electron scattering from a deeply bound nucleon on the light-front. *Physical Review C*, 98(3), Sep 2018.
- [5] T. De Forest. Off-Shell electron Nucleon Cross-Sections. The Impulse Approximation. *Nucl. Phys. A*, 392:232–248, 1983.
- [6] O. Hen, G. A. Miller, E. Piassetzky, and L. B. Weinstein. Nucleon-Nucleon Correlations, Short-lived Excitations, and the Quarks Within. *Rev. Mod. Phys.*, 89(4):045002, 2017.
- [7] R. Subedi et al. Probing Cold Dense Nuclear Matter. *Science*, 320:1476–1478, 2008.
- [8] Claudio Ciofi degli Atti. In-medium short-range dynamics of nucleons: Recent theoretical and experimental advances. *Phys. Rept.*, 590:1–85, 2015.
- [9] J. Carlson, S. Gandolfi, F. Pederiva, Steven C. Pieper, R. Schiavilla, K. E. Schmidt, and R. B. Wiringa. Quantum Monte Carlo methods for nuclear physics. *Rev. Mod. Phys.*, 87:1067, 2015.
- [10] J. Arrington, D. W. Higinbotham, G. Rosner, and M. Sargsian. Hard probes of short-range nucleon-nucleon correlations. *Prog. Part. Nucl. Phys.*, 67:898–938, 2012.
- [11] Leonid Frankfurt, Misak Sargsian, and Mark Strikman. Recent observation of short range nucleon correlations in nuclei and their implications for the structure of nuclei and neutron stars. *Int. J. Mod. Phys.*, A23:2991–3055, 2008.
- [12] O. Hen et al. Momentum sharing in imbalanced Fermi systems. *Science*, 346:614–617, 2014.
- [13] I. Korover et al. Probing the Repulsive Core of the Nucleon-Nucleon Interaction via the ${}^4\text{He}(e, e'pN)$ Triple-Coincidence Reaction. *Phys. Rev. Lett.*, 113(2):022501, 2014.
- [14] E. Piassetzky, M. Sargsian, L. Frankfurt, M. Strikman, and J. W. Watson. Evidence for the strong dominance of proton-neutron correlations in nuclei. *Phys. Rev. Lett.*, 97:162504, 2006.
- [15] N. Fomin et al. New measurements of high-momentum nucleons and short-range structures in nuclei. *Phys. Rev. Lett.*, 108:092502, 2012.
- [16] K. S. Egiyan et al. Measurement of 2- and 3-nucleon short range correlation probabilities in nuclei. *Phys. Rev. Lett.*, 96:082501, 2006.
- [17] L. L. Frankfurt, M. I. Strikman, D. B. Day, and M. Sargsian. Evidence for short range correlations from high Q^2 (e, e') reactions. *Phys. Rev.*, C48:2451–2461, 1993.
- [18] L. E. Marcucci, F. Sammarruca, M. Viviani, and R. Machleidt. Momentum distributions and short-range correlations in the deuteron and ${}^3\text{He}$ with modern chiral potentials. *Phys. Rev.*, C99(3):034003, 2019.
- [19] R. Cruz-Torres et al. Comparing proton momentum distributions in $A = 2$ and 3 nuclei via ${}^2\text{H}$, ${}^3\text{H}$ and ${}^3\text{He}$ ($e, e'p$) measurements. *Phys. Lett.*, B797:134890, 2019.
- [20] R. Cruz-Torres et al. Probing few-body nuclear dynamics via ${}^3\text{H}$ and ${}^3\text{He}$ ($e, e'p$)pn cross-section measurements. *Phys. Rev. Lett.*, in press, 2020.
- [21] F. Benmokhtar et al. Measurement of the ${}^3\text{He}(e, e'p)pn$ reaction at high missing energies and momenta. *Phys. Rev. Lett.*, 94:082305, 2005.

- [22] C. Ciofi degli Atti and L. P. Kaptari. On the interpretation of the processes ${}^3\text{He}(e, e'p){}^2\text{H}$ and ${}^3\text{He}(e, e'p)pn$ at high missing momenta. *Phys. Rev. Lett.*, 95:052502, 2005.
- [23] J. M. Laget. The Electro-disintegration of few body systems revisited. *Phys. Lett. B*, 609:49–56, 2005.
- [24] Leonid Frankfurt, Misak Sargsian, and Mark Strikman. Recent observation of short range nucleon correlations in nuclei and their implications for the structure of nuclei and neutron stars. *Int. J. Mod. Phys. A*, 23:2991–3055, 2008.
- [25] M. Alvioli, C. Ciofi degli Atti, and L. P. Kaptari. Calculation of the cross section and the transverse-longitudinal asymmetry of the process ${}^3\text{He}(e, e'p)pn$ at medium energies within the unfactorized generalized Glauber approach. *Phys. Rev.*, C81:021001, 2010.
- [26] Jacek Golak, Roman Skibiński, Henryk Witała, Walter Gloeckle, Andreas Nogga, H. Kamada Jagiellonian University Krakow, Ruhr U. Bochum, Forschungszentrum Juelich, and Kyushu Institute of Technology. Electron and photon scattering on three-nucleon bound states. *Physics Reports*, 415:89–205, 2005.
- [27] C. Carasco, J. Bermuth, P. Merle, P. Bartsch, D. Baumann, R. Böhm, D. Bosnar, M. Ding, Michael Distler, J. Friedrich, J. Golak, W. Glöckle, M. Hauger, Werner Heil, P. Jennewein, J. Jourdan, H. Kamada, Andi Klein, M. Kohl, and Markus Zeier. Final state interaction effects in ${}^3\text{He}(\vec{e}, e'p)$. *Physics Letters B*, 559:41–48, 04 2003.
- [28] M. Duer et al. Probing high-momentum protons and neutrons in neutron-rich nuclei. *Nature*, 560(7720):617–621, 2018.
- [29] D. Nguyen et al. Novel observation of isospin structure of short-range correlations in calcium isotopes. arXiv:2004.11448, 2020.
- [30] L.B. Weinstein et al. The CaFe Experiment: Isospin Dependence of Short-Range Nucleon Pairing in Nuclei, Proposal to Jefferson Lab PAC 45.
- [31] M. Duer et al. Direct Observation of Proton-Neutron Short-Range Correlation Dominance in Heavy Nuclei. *Phys. Rev. Lett.*, 122(17):172502, 2019.
- [32] E. O. Cohen et al. Center of Mass Motion of Short-Range Correlated Nucleon Pairs studied via the $A(e, e'pp)$ Reaction. *Phys. Rev. Lett.*, 121(9):092501, 2018.
- [33] C. Colle, O. Hen, W. Cosyn, I. Korover, E. Piasezky, J. Ryckebusch, and L. B. Weinstein. Extracting the mass dependence and quantum numbers of short-range correlated pairs from $A(e, e'p)$ and $A(e, e'pp)$ scattering. *Phys. Rev.*, C92(2):024604, 2015.
- [34] A. Schmidt et al. Probing the core of the strong nuclear interaction. *Nature*, 578(7796):540–544, 2020.
- [35] I. Korover et al. Tensor-to-Scalar Transition in the Nucleon-Nucleon Interaction Mapped by ${}^{12}\text{C}(e, e'pn)$ Measurements. arXiv:2004.07304, 2020.
- [36] Ronen Weiss, Betzalel Bazak, and Nir Barnea. Generalized nuclear contacts and momentum distributions. *Phys. Rev. C*, 92(5):054311, 2015.
- [37] R. Weiss, R. Cruz-Torres, N. Barnea, E. Piasezky, and O. Hen. The nuclear contacts and short range correlations in nuclei. *Phys. Lett.*, B780:211–215, 2018.
- [38] R. B. Wiringa, R. Schiavilla, Steven C. Pieper, and J. Carlson. Nucleon and nucleon-pair momentum distributions in $A \leq 12$ nuclei. *Phys. Rev. C*, 89:024305, Feb 2014.

- [39] J. Lachniet, A. Afanasev, H. Arenhövel, W. K. Brooks, G. P. Gilfoyle, D. Higinbotham, S. Jeschonnek, B. Quinn, M. F. Vineyard, G. Adams, and et al. Precise Measurement of the Neutron Magnetic Form FactorGMnin the Few-GeV² Region. *Physical Review Letters*, 102(19), May 2009.
- [40] S. Rock, R. G. Arnold, P. E. Bosted, B. T. Chertok, B. A. Mecking, I. Schmidt, Z. M. Szalata, R. C. York, and R. Zdarko. Measurement of elastic electron-neutron scattering and inelastic electron-deuteron scattering cross sections at high momentum transfer. *Phys. Rev. D*, 46:24–44, Jul 1992.
- [41] P. Markowitz et al. Measurement of the magnetic form factor of the neutron. *Phys. Rev. C*, 48(1):5–9, 1993.
- [42] E.E.W. Bruins et al. Measurement of the neutron magnetic form-factor. *Phys. Rev. Lett.*, 75:21–24, 1995.
- [43] H. Anklin et al. Precise measurements of the neutron magnetic form-factor. *Phys. Lett. B*, 428:248–253, 1998.
- [44] G. Kubon et al. Precise neutron magnetic form-factors. *Phys. Lett. B*, 524:26–32, 2002.
- [45] B. Anderson et al. Extraction of the neutron magnetic form-factor from quasi-elastic ${}^3\vec{\text{He}}(\vec{e}, e')$ at $Q^2 = 0.1\text{--}0.6 \text{ (GeV}/c)^2$. *Phys. Rev. C*, 75:034003, 2007.
- [46] Gerald A. Miller. Light front cloudy bag model: Nucleon electromagnetic form-factors. *Phys. Rev. C*, 66:032201, 2002.
- [47] M. Guidal, M.V. Polyakov, A.V. Radyushkin, and M. Vanderhaeghen. Nucleon form-factors from generalized parton distributions. *Phys. Rev. D*, 72:054013, 2005.
- [48] M. Diehl, Th. Feldmann, R. Jakob, and P. Kroll. Generalized parton distributions from nucleon form-factor data. *Eur. Phys. J. C*, 39:1–39, 2005.
- [49] C. Ciofi degli Atti and L. P. Kaptari. Calculations of the exclusive processes ${}^2\text{H}(e, e'p)n$, ${}^3\text{He}(e, e'p){}^2\text{H}$, and ${}^3\text{He}(e, e'p)pn$ within a generalized eikonal approximation. *Physical Review C*, 71(2), Feb 2005.
- [50] R. B. Wiringa, V. G. J. Stoks, and R. Schiavilla. Accurate nucleon-nucleon potential with charge-independence breaking. *Physical Review C*, 51(1):38–51, Jan 1995.
- [51] R. Machleidt. High-precision, charge-dependent bonn nucleon-nucleon potential. *Physical Review C*, 63(2), Jan 2001.
- [52] R. Cruz-Torres, D. Lonardoni, R. Weiss, N. Barnea, D. W. Higinbotham, E. Piassetzky, A. Schmidt, L. B. Weinstein, R. B. Wiringa, and O. Hen. Scale and Scheme Independence and Position-Momentum Equivalence of Nuclear Short-Range Correlations, 2019.
- [53] W. Bartel, F.W. Buesser, W.R. Dix, R. Felst, D. Harms, H. Krehbiel, P.E. Kuhlmann, J. Mcelroy, J. Meyer, and G. Weber. Electromagnetic form-factors of the neutron at squared four-momentum transfers of 1.0 and 1.5 (gev/c)-squared. *Phys. Lett. B*, 39:407–410, 1972.
- [54] H. Anklin et al. Precision measurement of the neutron magnetic form-factor. *Phys. Lett. B*, 336:313–318, 1994.
- [55] R. Cruz-Torres, D. Lonardoni, R. Weiss, N. Barnea, D. W. Higinbotham, E. Piassetzky, A. Schmidt, L. B. Weinstein, R. B. Wiringa, and O. Hen. Supplementary to scale and scheme independence and position-momentum equivalence of nuclear short-range correlations, 2019.

- [56] D Meekins. Hall A Tritium Target TGT-RPT-17-003. Technical report, Thomas Jefferson National Accelerator Facility, Newport News, 2017.
- [57] Andrew J Duncan and Michael J Morgan. Effect of Tritium on Cracking Threshold in 7075 Aluminum. Technical report, Savannah River National Laboratory, 2017.
- [58] S.N. Santiesteban, S. Alsalmi, D. Meekins, C. Ayerbe Gayoso, J. Bane, S. Barcus, J. Campbell, J. Castellanos, R. Cruz-Torres, H. Dai, T. Hague, F. Hauenstein, D.W. Higinbotham, R.J. Holt, T. Kutz, S. Li, H. Liu, R.E. McClellan, M. Nycz, D. Nguyen, B. Pandey, V. Pandey, A. Schmidt, T. Su, and Z. Ye. Density changes in low pressure gas targets for electron scattering experiments. *Nuclear Instruments and Methods in Physics Research Section A: Accelerators, Spectrometers, Detectors and Associated Equipment*, 940:351–358, oct 2019.
- [59] D. Meekins. TGT-CALC-103-010 Estimated Pressure In Tritium Cell and Permeation Rate. Technical report, Thomas Jefferson National Accelerator Facility, Newport News, Va, 2017.
- [60] H. M. HM M. HM Flower. Electron irradiation induced aqueous corrosion of aluminium and magnesium. *Radiation Effects*, 33(3):173–179, 1977.
- [61] S. Homan. HotSpot. <https://narac.llnl.gov/hotspot>, 2015.